On the Origin of Rotation Derived from Super Rapid Scan Satellite Imagery at the Cloud Tops of Severe Deep Convection

JASON M. APKE[a] AND JOHN R. MECIKALSKI[b]

[a] *Cooperative Institute for Research in the Atmosphere, Colorado State University, Fort Collins, Colorado*
[b] *Department of Atmospheric Science, University of Alabama in Huntsville, Huntsville, Alabama*

(Manuscript received 26 June 2020, in final form 22 March 2021)

ABSTRACT: Severe thunderstorms routinely exhibit adjacent maxima and minima in cloud-top vertical vorticity (CTV) downstream of overshooting tops within flow fields retrieved using sequences of fine-temporal-resolution (1-min) Geostationary Operational Environmental Satellite (GOES)-R series imagery. Little is known about the origin of this so-called CTV couplet signature, and whether the signature is the result of flow-field derivational artifacts. Thus, the CTV signature's relevance to research and operations is currently ambiguous. Within this study, we explore the origin of near-cloud-top rotation using an idealized supercell numerical model simulation. Employing an advanced dense optical flow algorithm, image stereoscopy, and numerical model background wind approximations, the artifacts common with cloud-top flow-field derivation are removed from two supercell case studies sampled by GOES-R imagers. It is demonstrated that the CTV couplet originates from tilted and converged horizontal vorticity that is baroclinically generated in the upper levels (above 10 km) immediately downstream of the overshooting top. This baroclinic generation would not be possible without a strong and sustained updraft, implying an indirect relationship to rotationally maintained supercells. Furthermore, it is demonstrated that CTV couplets derived with optical flow algorithms originate from actual rotation within the storm anvils in the case studies explored here, though supercells with opaque above-anvil cirrus plumes and strong anvil-level negative vertical wind shear may produce rotation signals as an artifact without quality control. Artifact identification and quality control is discussed further here for future research and operations use.

KEYWORDS: Clouds; Convection; Cloud tracking/cloud motion winds; Remote sensing; Satellite observations; Mesoscale models; Vorticity

1. Introduction

Rotating deep convection (DC) is associated with all modes of severe weather at the ground (e.g., flooding, strong winds, large hail, tornadoes; Byers and Braham 1949; Lemon and Doswell 1979). Given impacts to life and property, considerable research efforts have been made toward collection of DC kinematic observations from fixed ground-based Doppler radar (e.g., Browning 1964, 1965; Marwitz 1972; Brandes 1977, 1978, 1984; Markowski 2002 and references within), mobile and dual-polarization radar (e.g., Bluestein et al. 1995, 2010; Wurman et al. 1997; Kumjian and Ryzhkov 2008; French et al. 2014), lightning detection systems (e.g., Williams et al. 1999; Deierling and Petersen 2008; Schultz et al. 2009, 2011, 2015; Stough et al. 2017), and geostationary satellite imagery (Fujita 1982; Bedka et al. 2010; Bedka and Khlopenkov 2016; Bedka et al. 2018; Griffin et al. 2016). Recent experiments show that storm-scale rotation (wavelengths $< \sim 20$ km) present in some DC cloud tops is now objectively derivable with new fine-temporal-resolution Super Rapid Scan (SRS; ≤ 1 min) Geostationary Operational Environmental Satellite (GOES)-R series imagery loops (Apke et al. 2016, 2018, hereafter A16 and A18). The rotation is sometimes presented as a pair of strong vortices downstream of overshooting tops (OTs), which can last for several hours (Fig. 1). A16 referred to this phenomenon as a cloud-top vorticity (CTV) "couplet" (CTVC), and such couplets are routinely evident with *GOES-16* SRS imagery of supercells.

The origin of the CTVC is currently unknown, and recent large-sample studies, which utilized this objectively derived flow find no obvious statistical relationship with the magnitude of CTV and the occurrence of severe weather at the ground (e.g., Sandmæl et al. 2019; Mecikalski et al. 2021). This implies that CTV may not be directly coupled with the low- to midlevel processes of the storm that are conducive to severe weather development, or that the relationship between the two is nonlinear, and hence is not fully understood. It is also possible that CTVCs are at least partially an artifact (or optical illusion) of top-down geostationary observation, which is not accounted for in current cloud-top flow-field (CTFF) derivation methods (more in section 2). The lack of understanding in the origin and artifacts of derived CTV yields ambiguity in interpretation of the satellite imagery, and, by extension, uncertainty in how recognition of this CTVC signature would be useful in an operational setting.

Therefore, we aim to explore two primary questions: 1) Where does the actual CTV present over DC originate, and 2) What are possible artifacts that impact our capability to derive the CTV over DC using satellite imagery? In addressing these questions, we can move closer toward using retrieved CTFF properties over DC to better understand the relationships to internal updraft kinematics such as rotation and inferred updraft strength. To explore question 1, an idealized supercell simulation is used, which produces vertical vorticity (ζ) near the cloud top as shown in A16. Question 2 is addressed with image stereoscopy and advanced optical flow retrievals, designed to

Corresponding author: Jason Apke, jason.apke@colostate.edu

DOI: 10.1175/MWR-D-20-0209.1

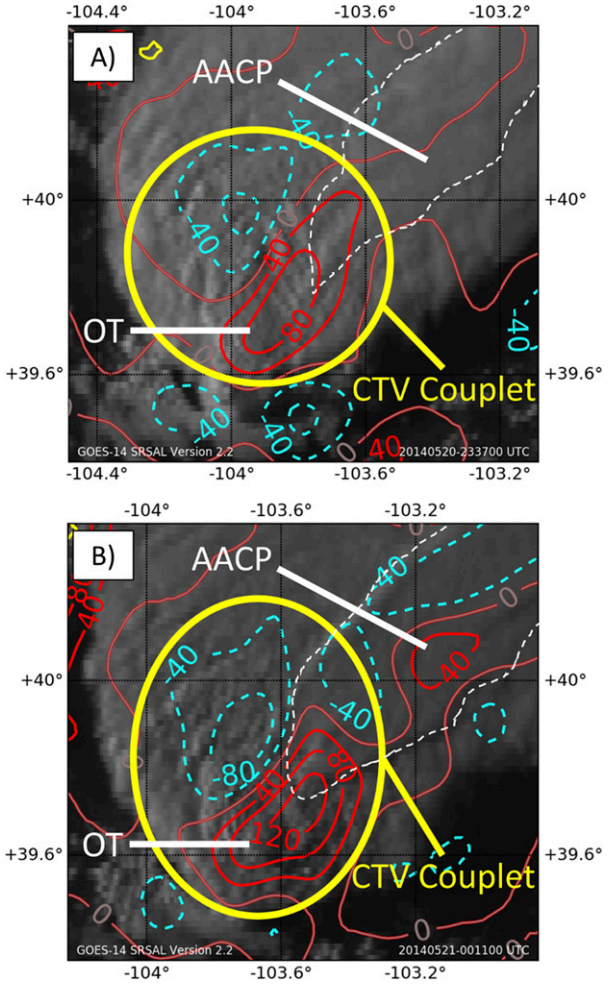

FIG. 1. *GOES-14* super rapid scan operations for GOES-R visible 0.64-μm reflectance shown for (a) 2337 UTC 20 May and (b) 0011 UTC 21 May 2014 over a supercell in central Colorado with positive (negative) derived CTV following A18 contoured in red (cyan) every 40 $\times$ 10^{-5} s^{-1}. Also highlighted are the overshooting top (OT) and above-anvil cirrus plume (white dashed line; AACP) features (cf. A16, Fig. 12).

mitigate flow-field artifacts found in A16 and A18, over two CTVC-producing supercells sampled by GOES-R imagers.

The background in GOES-based CTFF retrieval is presented in section 2. Section 3 describes the simulation used to explore the origin of CTV and presents a new method of CTFF computation. The results are presented in section 4. Sections 5 and 6 discuss and conclude the study to show the CTVC origin, which should impact how CTFFs could be used for inferring internal DC kinematics in the future.

2. Background

a. Objective flow derivation in imagery

In previous studies, CTFFs over DC are derived with satellite imagery using three fundamental steps: 1) objectively track features of interest through a GOES imagery sequence to obtain point-source atmospheric motion vectors (AMVs), 2) identify AMVs in clouds that are above a permissible altitude, and 3) assuming the retained AMVs exist on a flat plane, perform objective analysis to retrieve u- and v-wind components over a grid (A18). Step 3 requires spatially dense, high-quality motion vectors from step 1 to produce storm-scale ($<\sim$20 km) flow. With most AMV derivation schemes, which implement strict target quality control checks prior to feature tracking (Nieman et al. 1997; Bedka and Mecikalski 2005; Bresky et al. 2012), very short time steps between satellite images are needed to retrieve dense enough flow fields (e.g., $\leq$1-min; A16). Quality control checks within operational schemes can also be relaxed to further supplement AMV density with wind estimates that deviate from synoptic-scale background numerical model estimated flow, which are so-called mesoscale AMVs (mAMVs; Bedka and Mecikalski 2005).

Two main problems are encountered when the traditional AMV retrieval methods (steps 1–3) are applied over DC. First, the flat plane assumption in step 3 fails to account for the multi-cloud-layer scenes that are possible over and around severe DC. A16 reported multiple instances where multilayer cloud scenes resulted in likely nonsensical cloud-top divergence (CTD) and CTV estimates with the above three-step approach. Second, step 3 smooths over (and computes derivatives across) what are essentially natural ''motion discontinuities'' in satellite imagery loops (e.g., Black and Anandan 1996). Motion discontinuities are not accounted for within any operational AMV algorithm today. The Derived Motion Vector system (DMVs; Bresky et al. 2012) that is used to generate operational AMV fields with GOES-R series imagery, for example, tracks small targets (5 pixels $\times$ 5 pixels) within a large target area (15 pixels $\times$ 15 pixels) using sum-of-square error minimization. The small-target motions are clustered to find the dominant derived displacement in the large target area, and the dominant motion pixels are used for improved AMV height assignments. By ignoring the nondominant pixels within the image scene, Bresky et al. preserve the possibility of multiple flows (e.g., pixels within a target region that move in different directions) in the large target area (a significant improvement over previous systems), though discontinuities and multiple flows are still not preserved within the small targets.

The computer vision community addresses the multiple motions and discontinuities with more advanced so-called optical flow computation methods (e.g., Horn and Schunck 1981; Black and Anandan 1996; Sun et al. 2014). AMVs represent one subset of optical flow methods, ordinarily considered ''patch matching'' schemes, dating back to the work by Fujita (1968). These schemes require trackable targets (e.g., Shi and Tomasi 1994) to function, and hence cannot produce accurate ''dense'' motion fields in satellite imagery (where motion is computed at every image pixel; Nieman et al. 1997). Some advanced optical flow techniques derive dense motion fields by minimizing (or optimizing) ''energy'' functions, comprised of a few assumptions on motion smoothness and brightness behavior over time, where reasonably accurate estimates of motion can be made even in image areas with little to no texture (see appendix A). One of these newer techniques is adopted here. Optical flow derivation is currently a rapidly

evolving field, and for recent comprehensive reviews on the past and latest techniques, the reader is referred to works by Barron et al. (1994), Fleet and Weiss (2005), and Fortun et al. (2015).

b. DC cloud-top rotation illusions and origins

A phenomenon downstream of OTs that may cause motion discontinuities and the "optical illusion" of the CTVC is the above-anvil cirrus plume (AACP; McCann 1983; Brunner et al. 2007), where gravity wave breaking near an OT injects ice crystals downstream into the upper troposphere and lower stratosphere (Wang 2003, 2007). These ice crystals form a thin veil that can reside several kilometers above a DC anvil (Wang 2004; Wang et al. 2016) and may have different horizontal flow properties than the outflow within the primary anvil. AACPs are common over severe DC (Bedka et al. 2015, 2018). However, the complex shape, size, transparency, and magnitude of infrared (IR) brightness temperature differences within an AACP, relative to the main cumulonimbus anvil, makes objective identification challenging. Therefore, large statistical analyses predicated on AACP identification in storms typically require some subjective input (Brunner et al. 2007; Bedka et al. 2018).

If an AACP is present and moves slower than the main anvil, the storm may appear to be rotating from a top-down perspective. The three-step approach in section 2a would mix the anvil and AACP flows together, resulting in vortices that are an artifact of the product (and the appearance of a CTVC) and not a physical trait of the storm. Fujita (1982) documented the DC CTFF appearance from a top-down perspective using Lear jet observations of an AACP producing storm (see Fig. 1 in Fujita 1982), and the resemblance to CTVCs cannot be denied. He hypothesized the CTFF found is the result of negative environmental vertical wind speed shear between the primary anvil and the AACP, which, in his case, was several kilometers above the surrounding anvil. This artifact is hereafter referred to as the "vertical shear artifact." This vertical shear artifact implies that the AACP, not internal rotation within supercells, is the cause of what is objectively derived in A16. The vertical shear artifact also implies that derived CTD is underestimated when AACPs downstream of the OT are present, which may cause statistical overlap in storm intensity populations when using CTD to distinguish between weak and strong updrafts (as in A18).

Closer to the OT, large spurious rotation signatures may occur due to oversmoothing of multilayer-cloud-scene flow, especially in the cases of horizontally small anvils where the ground or lower-level pixels are spatially close to the ζ maxima and incorrectly height-assigned in the second step of the three-step approach. We refer to this phenomenon as the "anvil-edge artifact." It is simple to spot apparent rotation along an anvil edge in case-by-case analyses such as A16 and A18. Large sample statistical studies (e.g., Sandmæl et al. 2019; Mecikalski et al. 2021), however, are susceptible to misrepresenting derived CTV as related to severe weather because of anvil edges, specifically when the maximum CTV is recorded within a certain radius of the OT. The anvil-edge artifact therefore could explain some statistical overlap between the CTV of severe versus nonsevere storms.

In contrast, not all CTVCs appear to be caused by the artifacts described above. The 20 May 2014 supercell over central Colorado in A16 and shown in Fig. 1 is one such example (see section 4c in A16 and Fig. 12). The CTVC was far away from the cloud edge, and the AACP in the storm was not oriented along the maxima in rotation (see the white dashed line in Fig. 1a). Moreover, this ζ signature was also present near the cloud top of a simple idealized Weather Research and Forecasting (WRF) Model simulation within A16. These CTVCs have a remarkable resemblance to the midlevel structure of supercells (e.g., Lemon and Doswell 1979; Klemp 1987). As is well known, the midlevel rotation in supercells initially occurs due to the tilting, and subsequent stretching of preexisting horizontal vorticity ($\boldsymbol{\omega}_h$) in an environment with vertical wind shear (Weisman and Klemp 1982, 1984; Klemp 1987). A16 found through an Eulerian vorticity equation budget analysis (at one near-cloud-top level) that tilting, stretching, and advection were the primary generation mechanisms of ζ observed. This approach did not capture the source of rotation at the cloud top, which would require a backward-trajectory (Lagrangian) analysis instead.

Trajectories have long been used to identify the origins of rotation associated within the midlevels (mesocyclones; Klemp et al. 1981; Rotunno and Klemp 1985) and low levels (tornadoes; Wicker and Wilhelmson 1995; Adlerman et al. 1999; Mashiko et al. 2009; Schenkman et al. 2014; Betten et al. 2017) of DC in numerical simulations. The tornado's convergent and intense rotation means backward trajectories (trajectories integrated backward in time) are susceptible to large discretization-related location errors with long time steps and low gridpoint spacing in modeled data (Dahl et al. 2012). Dahl et al. (2012) also noted that the forward trajectories tested had less spatial error owing to their initial positions within the better-resolved flow and the confluent nature of the trajectories with time. From this result, we infer that the analogous backward trajectories within divergent phenomena, such as the outflow near the top of DC, are less susceptible to displacement error, which is ideal for use in this present study.

Trajectory analyses have not been used to analyze the flow structure of the cloud tops of supercells, which produce AACPs and CTVCs. We investigate the CTV in a numerical weather prediction (NWP) model in comparison to motion derived from case studies using a dense optical flow (DOF) scheme tailored to the problem at hand introduced in the next section.

3. Methodology

a. Derivation of cloud-top flow

To track brightness features objectively in GOES-R-era imagery loops, we use a modified DOF derivation technique presented by Sun et al. (2014), with a summary of the derivation and settings shown in appendix A. We selected this system due to its simplicity, excellent documentation, and availability of open-source information, though DOF validation experiments are currently underway to determine the best practices in terms of constraints and regularizers for satellite meteorology applications. For comprehensive validation comparisons

on more general applications of new and emerging DOF derivation techniques, the reader is referred to the Middlebury (Baker et al. 2011), Max-Planck Institute (MPI)-Sintel (Butler et al. 2012), and Karlsruhe Institute of Technology and Toyota Technological Institute at Chicago (KITTI; Geiger et al. 2012) benchmark datasets.

We achieve steps 2 and 3 and remove common noise from the DOF output using a bilateral filter at each point, where

$$[\hat{u},\hat{v}] = \frac{\sum_{i,j\in N_s} w_{i,j} \times [u,v]}{\sum_{i,j\in N_s} w_{ij}},$$

$$w_{i,j} = \exp\left\{-\frac{|i_c - i|^2 + |j_c - j|^2}{2\sigma_1^2} - \frac{|T_{b_c} - T_{b_{i,j}}|^2}{2\sigma_2^2}\right\}. \quad (1)$$

The resulting field values of $\hat{u}$ and $\hat{v}$ are a weighted average of the DOF dependent on the distance of the pixel within the neighborhood N_s from the center at $x = [i_c, j_c]$ and the difference between 10.3-μm brightness temperatures (T_b). Prior to bilateral smoothing in Eq. (1), the DOF u and v fields are averaged temporally over a 5-min period. We correct for 0–6 km storm motion using Bunkers et al. (2000) within this temporal averaging step with the analysis hour winds from the Rapid Refresh model (RAP; Benjamin et al. 2016) acquired from the National Centers for Environmental Information archive (NCEI 2021). The DOF u and v quantities from previous time frames at the storm-motion corrected locations are collected with bilinear interpolation. The constants σ_1 and σ_2 change the relative importance of distance and T_b differences in the bilateral filter, respectively, and are set to 9 (VIS image) pixels and 20 K. With a neighborhood size of 32 × 32 pixels, we recover a CTFF with similar frequency responses of filters used in A16 and A18. Finite differencing is then used to retrieve CTD and CTV over the grid, masking out any pixels with excessive T_b differences (>5 K) across pixels that are finite differenced, on the following case studies.

b. Case study analysis

Two case study times are considered here: 2059 UTC 28 July 2018 and 2202 UTC 29 May 2019. Both time frames are periods when severe thunderstorms in the United States produced AACP signatures and were identified to have CTVCs (Fig. 2). Furthermore, each storm was long lived (>1 h) and had apparent mesocyclones associated with their primary updrafts (Fig. 3), which fits standard definitions of supercells (e.g., Davies-Jones et al. 2001). The first case study was sampled by *GOES-16* in orbit at 75.2°W and *GOES-17* in the checkout position at 89.5°W. *GOES-17* was in the operational position at 137°W for the second case study. Each satellite collected VIS (~1 km at nadir) and IR (~2 km at nadir) imagery once every 1 min within 1000 km × 1000 km sectors (so-called mesoscale sectors; Schmit et al. 2017) and once every 5 min in contiguous U.S. (CONUS) sectors (“mode 3”). The times were selected when the CONUS sector from the complementary satellite overlapped the mesoscale sector scans used within 30 s (at scan time). This temporal overlap is necessary for accurate multi-satellite-image stereoscopy (e.g., Hasler 1981). CTFFs were computed using the mesoscale sector 0.64-μm VIS channel on *GOES-16* (*GOES-17*) for the first (second) case study. The AACPs were then manually identified using the VIS and IR imagery (following Bedka et al. 2018).

Our goals with the two case studies are to explore: 1) the vertical shear and anvil edge artifacts, and 2) determine whether they are present. With the DOF derivation scheme used, the mAMV and objective analysis scheme mitigates smoothing across the anvil-edges (drastically reducing the anvil-edge artifact). If the AACPs are opaque in VIS imagery, the DOF schemes will also produce motion discontinuities along the AACP edge prior to bilateral and temporal smoothing if the vertical shear artifact is present. If the CTVC is present in the smoothed DOF fields without a motion discontinuity in the raw CTFFs along the AACP edge, then the CTVC is not an artifact of the CTFF objective analysis scheme.

Of note, the vertical shear artifact may still exist within the DOF derivation itself as the assumptions in the Sun et al. (2014) scheme break down (and motions are mixed) in some transparent scene cases. The maximum CTV related to the vertical shear artifact is thus quantified here by: 1) determining the cloud-top height (CTH) of the AACP and the primary DC anvil, 2) determining the background environmental wind at the AACP and anvil altitude, and 3) recomputing the smoothed CTFFs with the background wind removed from the AACP and the anvil.

The first step is achieved with manual image stereoscopy described in appendix B. For the second step, we use an average height for the primary anvil level and the maximum height for the AACP to determine the background wind (also taken from RAP). For the third step, we subtract the RAP winds from the maximum AACP altitude where the AACP was identified, and the average anvil-level everywhere else. In each case, the RAP has a ~1.2-km vertical resolution at the anvil altitude (and does resolve negative vertical wind shear above the anvil), and linear interpolation is used here to approximate the background flow at subpixel scale. The residuals between the original and new CTV field will show the maximum possible CTV caused by the vertical shear artifact within the case studies used. The observations of the flow within AACPs, and the flow fields observed around the AACPs, are then compared to NWP simulations of idealized supercells.

c. Model configuration

The WRF-Advanced Research WRF (ARW; Skamarock et al. 2008) version 4.1.1 was used to simulate AACP and CTVC producing DC. Following Homeyer et al. (2017), the Weisman and Klemp (1982) sounding (and quarter-circle hodograph) is used as a horizontally homogeneous environment with model settings defined in Table 1. The horizontal grid-point spacing is less than 1 km as suggested by Bryan et al. (2003) to better resolve turbulence and entrainment within DC. Two changes are applied to the environment for this simulation from the original Weisman and Klemp (1982) setup. First, the simulation uses wind speeds that are 25% greater than the original quarter circle hodograph. Storm motion

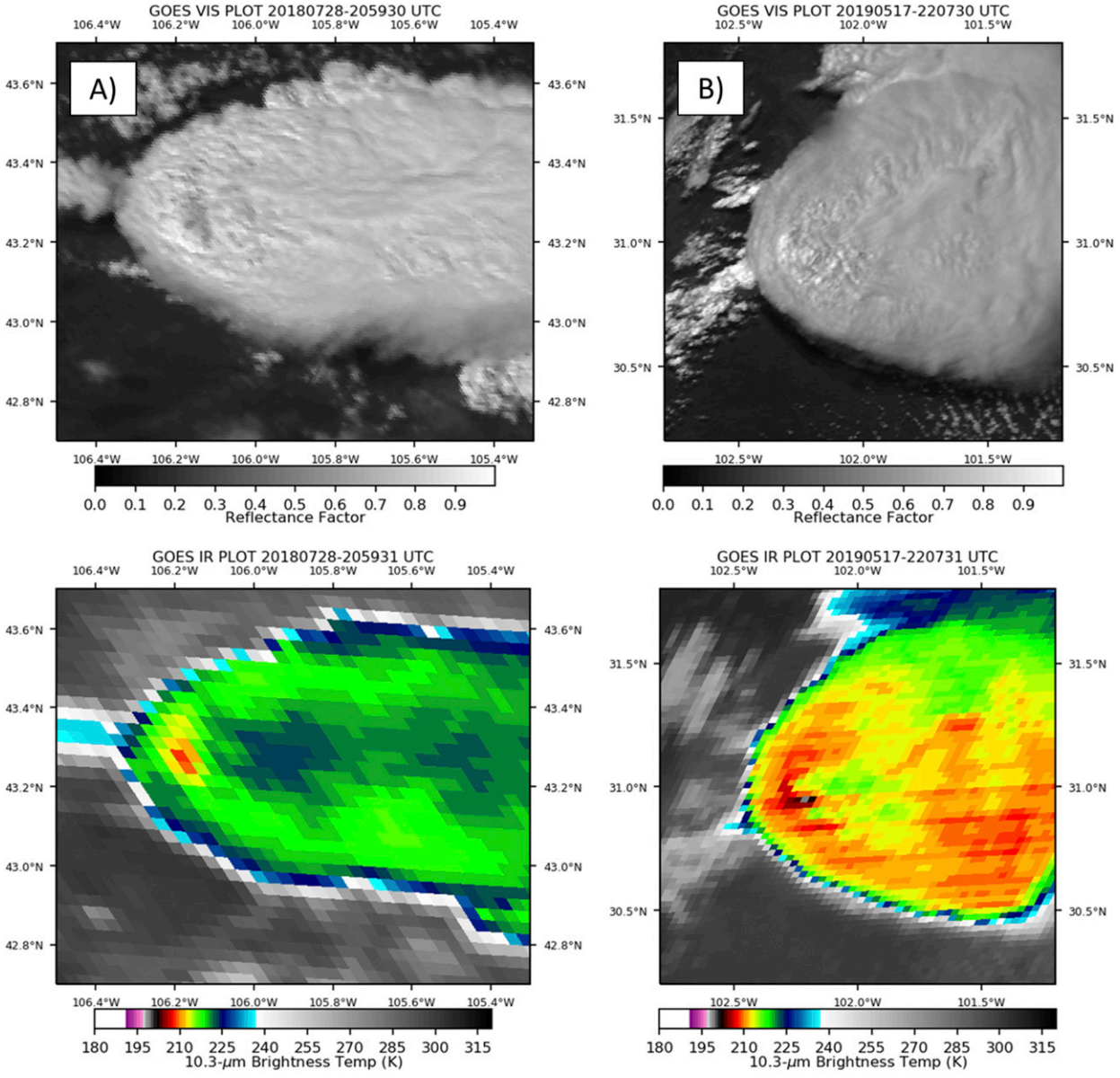

FIG. 2. (top) *GOES-16* 0.64-μm VIS imagery and (bottom) 10.3-μm brightness temperature shown for (a) 2100 UTC 28 Jul 2018 supercell over central Wyoming and (b) 2207 UTC 17 May 2019 supercell over central Texas. The reader should note that the ABI on the *GOES-17* was found to have a cooling system issue that diminishes the accuracy of scan lines in IR and water vapor imagery when the sun shines directly toward the imager. The issue does not impact visible image channels used for optical flow computation, and, while present in the 10.3-μm imagery here, was not significant enough to obscure relevant features for the case studies examined here.

computed using Bunkers et al. (2000) is also subtracted from all levels of the hodograph to keep the storm within the domain during the entire simulation. Second, the water vapor mixing ratio in the idealized profile is decreased to 5 ppmv ($\sim 3.11 \times 10^{-3}$ g kg^{-1}) in the first 2 km of the stratosphere (consistent with Homeyer et al. 2017).

d. Trajectory analysis

The origin of rotation in the near-cloud-top DC anvil and the AACP is determined by tracking parcels that acquire rotational momentum backward in time. This involves first identifying regions of strong ζ within the AACP and OT and tracking parcels within that grid back to their source region. Backward trajectories are found using the flow within the WRF-ARW model with 1 s history output. Flow values (u, v, w), pressure, and density are derived at each parcel location with trilinear interpolation. Consistent with Betten et al. (2017), the gradients are found using cubes centered around each parcel location with a fourth-order centered finite-differencing scheme. Linear interpolation is used between

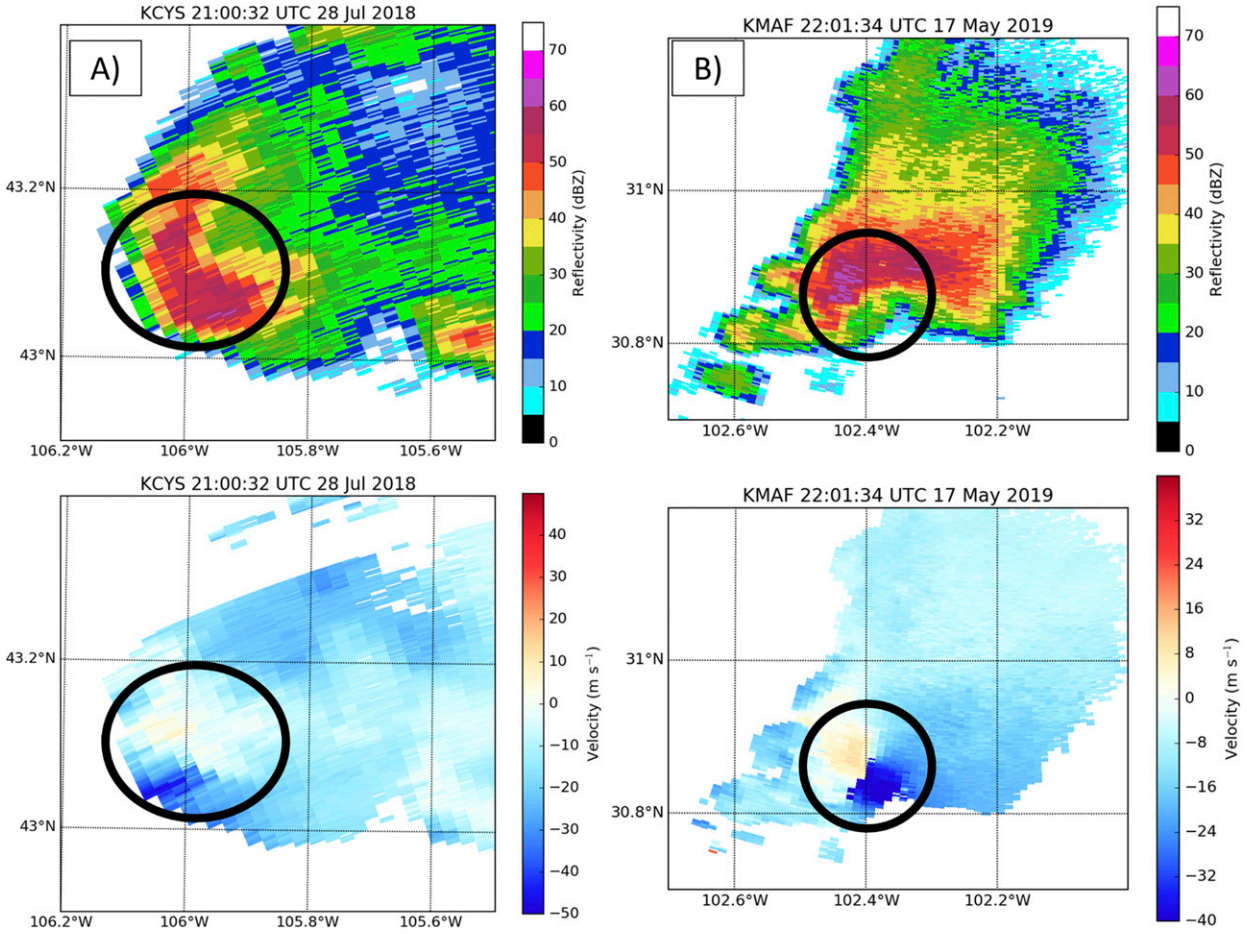

FIG. 3. The Weather Surveillance Radar-1988 Doppler (WSR-88D) (top) reflectivity and (bottom) radial velocity from (a) 2100 UTC 28 Jul 2018 0.5° tilt scan from the Cheyenne, WY, site (KCYS) and (b) the 2201 UTC 17 May 2019 1.3° tilt scan from the Midland, TX, site (KMAF). The apparent mesocyclone is highlighted in each image within the black circle. Radar velocities within these plots were manually de-aliased using the SOLO-III system (Oye et al. 1995) and all plots were created using the Python Atmospheric Radiation Measurement (ARM) Radar Toolkit (Py-ART) software (Helmus and Collis 2016).

time frames to acquire flow updates every 0.5 s, and trajectories are advanced backward in time with an Euler integration scheme.

Along the trajectory path, the individual components of the vorticity tendency within the model are integrated following the 3D vorticity equation:

$$\frac{d\boldsymbol{\omega}}{dt} = \underbrace{(\boldsymbol{\omega}\cdot\nabla)\mathbf{v}}_{A} \underbrace{-\boldsymbol{\omega}(\nabla\cdot\mathbf{v})}_{B} \underbrace{-\nabla\alpha\times\nabla p}_{C} \underbrace{+\nabla\times\mathbf{F}}_{D}, \qquad (2)$$

where $\boldsymbol{\omega} = [\omega_x, \omega_y, \zeta]$ represents a vector containing x, y, and z components of vorticity, $\mathbf{v}$ contains the x, y, and z components

TABLE 1. Settings used for the idealized supercell WRF-ARW simulation.

WRF-ARW parameter	Setting
Domain size (x, y, z); No. of vertical levels	84 km, 84 km, 25 km; 141
Gridpoint spacing (x, y, z)	500 m, 500 m, ~180 m
Integration time step	1 s
Total run time	90 min
Microphysics	Mansell et al. (2010)
Advection schemes	Horizontal fifth order, vertical third order
Turbulence closure	Smagorinsky (1963)
Damping layer size	5 km
Bubble size (x, y, z)	10 km, 10 km, 1.5 km
Bubble temperature perturbation	3 K

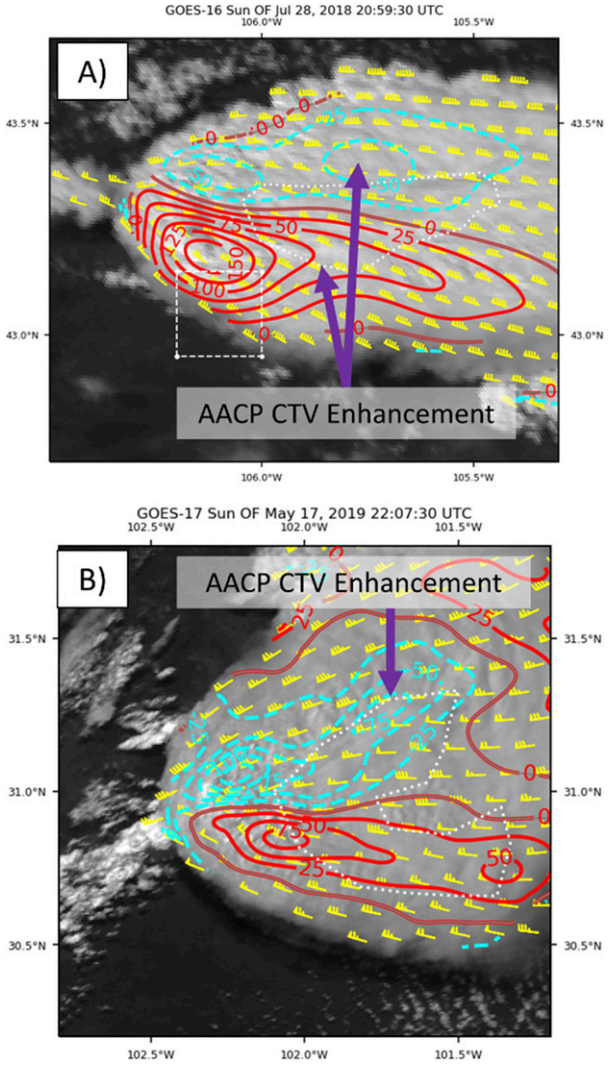

FIG. 4. (a) The 2059 UTC 28 Jul 2018 *GOES-16* and (b) the 2207 UTC 17 May 2019 *GOES-17* 0.64-μm VIS imagery with CTV contoured with positive (negative) values shown in red (cyan dashed) every 25×10^{-5} s^{-1} and AACP locations highlighted with a dotted white line.

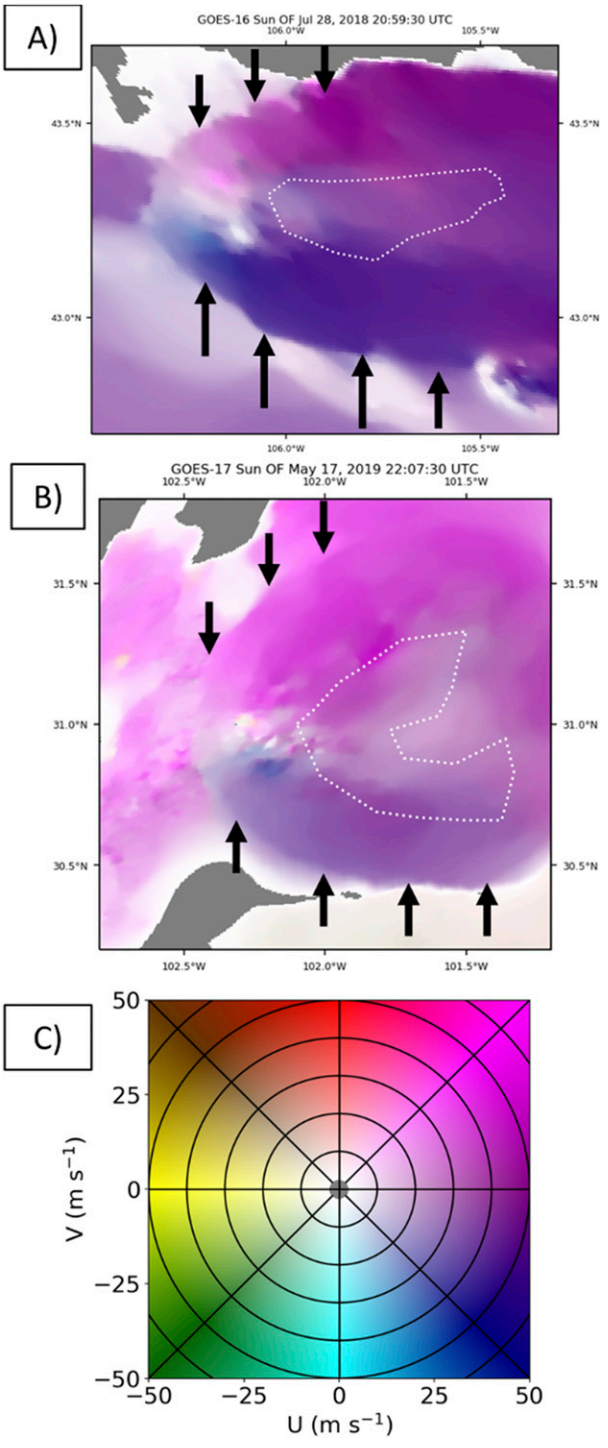

FIG. 5. Color-shaded optical flow plot for (a) the 2059 UTC 28 Jul 2018 and (b) the 2207 UTC 17 May 2019 case studies shown with motion discontinuities highlighted with black arrows. (c) The color scale used in (a) and (b).

of flow, α is the specific volume, p is the pressure, and $\mathbf{F} = [F_u, F_v, F_z]$ is a vector containing the forces related to numerical diffusion, Rayleigh dampening, and the turbulence scheme. Therefore, term A is the tilting term, term B is the stretching term, term C is the baroclinic generation or solenoidal term, and term D represents viscous effects (hereafter referred to as the diffusion term). The left-hand side of the equation is the sum of the local rate of vorticity change and the advection, representing the Lagrangian change in vorticity. Integration for terms is done at each trajectory time step with a fourth-order Runge–Kutta integration scheme to mitigate integration errors in exponential vorticity growth.

Initial trajectory locations are selected within the generated CTVC over the AACP and OT to determine the parcel origins, and how these near-cloud-top flows relate to the internal updraft structure. Trajectories within 10×10 boxes in regions of interest are tracked to avoid reaching conclusions with only one flow that may not represent what is present in an area. The

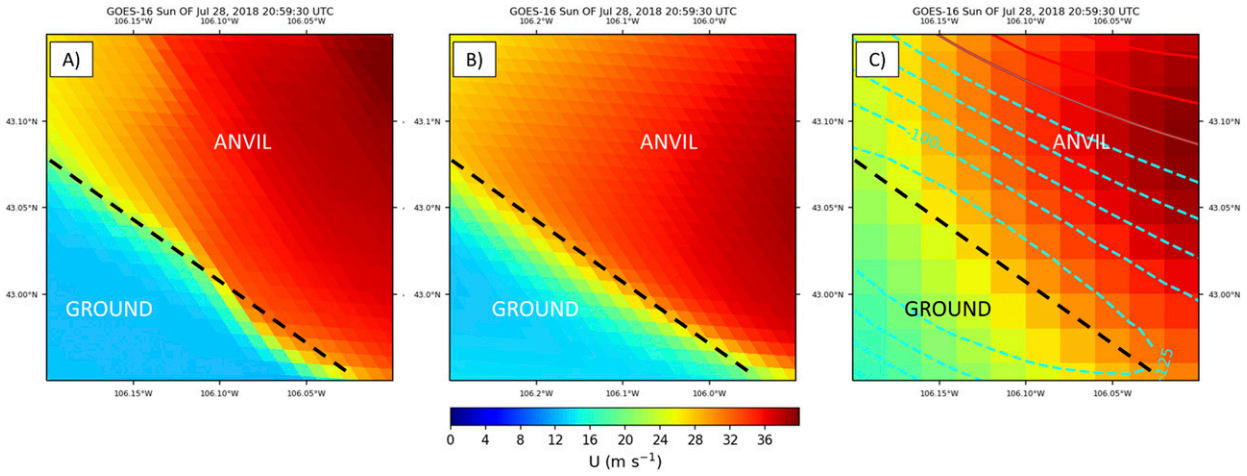

FIG. 6. Color-shaded u wind speed (m s^{-1}) within the white box shown in Fig. 4a from (a) the 2059 UTC 28 Jul 2018 raw optical flow, (b) the bilaterally smoothed optical flow field, and (c) the optical flow field smoothed following the recursive filter outlined in A18 shown with contours of the CTV using that field with positive (negative) values contoured in red (cyan dashed) every 25×10^{-5} s^{-1}. Note that in (c) we include all vectors, not just those above 500-hPa altitude, to highlight the anvil-edge artifact. The black dashed line is a reference to separate the ground from the anvil-level flow.

trajectories are tracked for 30 min backward in time to adequately capture parcel origins.

4. Results

a. AACP impact on cloud-top flow

The 28 July 2018 case study exhibits large CTV upstream of the AACP and enhanced CTV along the AACP edge (Fig. 4a). The 17 May 2019 case study also exhibits enhanced anticyclonic CTV, which extends northeastward along the AACP edge in a manner not observed in numerical simulations within A16 (Fig. 4b). The maximum CTV magnitudes for each case study ($>1.25 \times 10^{-3}$ s^{-1}) were larger than the CTV in the AACP-enhanced regions and located just upstream of the AACPs. Despite the enhancements in CTV, the raw DOF fields have no obvious (or temporally consistent) motion discontinuities between the anvil and AACP for either case study (Figs. 5a,b). Sharper discontinuities are observed on the primary anvil edges, where larger horizontal shear exists between cloud layers. These anvil edge discontinuities are importantly preserved with the bilateral smoothing used here (Figs. 6a,b), compared to the recursive filter approach used in A18 on the same optical flow field, which smooths multilayer motions together and yields unrealistic anticyclonic motion within the anvil (an example of the anvil-edge artifact; Fig. 6c). Careful examination of 1-min animations from each case study implies that each AACP was transparent in the VIS imagery used for DOF computation. The apparent AACP-edge CTV enhancements, however, imply mixing of motions in the DOF derivation between each cloud layer.

The stereoscopy derived CTH for each case study indicates that the AACPs were, at most, ~2 km above the surrounding anvils downstream of the OT (Fig. 7). The anvil-level (AACP) flow for 28 July 2018 and 17 May 2019 acquired from RAP model data were $u = 40$ m s^{-1}, $v = -14.5$ m s^{-1} ($u = 24$ m s^{-1}, $v = -8$ m s^{-1}) and $u = 34$ m s^{-1}, $v = 4$ m s^{-1} ($u = 8$ m s^{-1}, $v = -2$ m s^{-1}), respectively. These winds assume the worst-case scenario (with negative vertical wind shear) for AACP height and motion. Subtracting the background winds for 28 July 2018 more than removes the apparent enhancement of CTV caused by vertical wind shear, and increases the overall CTD, particularly near the AACP upstream edge (Fig. 8). In relation to typical CTV magnitudes, the worst-case enhancement appears to add close to ~80% of observed CTV magnitude maxima well downstream of the OT (Fig. 8d). The CTD maximum is reduced by ~35%, which implies that CTD maxima over the OT are less susceptible to the vertical shear artifacts, so long as the AACP is downstream of the OT and the viewing angle permits flow derivation over the OT.

Removing the background winds from 17 May 2019 dampens the anticyclonic CTV east of the OT; however, it also adds cyclonic CTV and anticyclonic CTV where it does not appear to occur in the image loop (Fig. 9). The CTD reduction was larger (~43% reduction relative to the maxima observed; Figs. 9a,c) with more negative vertical wind shear between the primary anvil and AACP, but still less than the relative CTV enhancement (closer to 60% enhancement of maxima/minima observed; Figs. 9b,d). Counterrotating CTV is also still observed within the AACP area in this case. At this point, it is also important to note that background flow removal did not entirely remove the CTVC signature in either case. The removal instead highlights the large maxima that occur immediately downstream of the OT. With both the anvil edge and vertical shear artifacts removed, the remaining presence of the CTVC implies that the rotation derived from the imagery comes from within the storm itself. The next question to answer is where

this observed actual (versus artifact) CTV originates, which we explore with the WRF-ARW model.

b. Trajectory analysis

Consistent with Homeyer et al. (2017), the idealized supercell produces a well-defined AACP at 90 min into the WRF-ARW simulation (Fig. 10). The OT, at $x = \sim 43$ km, $y = \sim 47$ km, is located upstream of the AACP, which extends from $x = \sim 46$ km, $y = \sim 50$ km to the domain edge at $x = y = 80$ km. Cyclonic and anticyclonic ζ is observed in the primary anvil (Fig. 11a) and AACP (Fig. 11b) of this simulation. The backward trajectories were selected to explore the formation of the ζ within and downstream of the OT and within the AACP (Table 2; Boxes in Figs. 10 and 11a,b). As shown in the previous section, it is likely that part of this ζ is the cause of the CTVC signature found with DOF techniques. Trajectories in boxes A and D represent the cyclonic and anticyclonic ζ within the AACP, and likely represent the cause of CTV that is derived well downstream of the OT. Trajectories in boxes B and C represent the cyclonic and anticyclonic ζ immediately downstream of the OT in the primary anvil (starting at a lower altitude than trajectories A and D), which is likely representative of the CTV magnitude maxima found in the last section. Trajectories in box E are within the OT at the same level as B and C, representing the weaker cyclonic CTV within the updraft itself. The following discussion overviews the origin of ζ within each of these trajectory regions and highlights the contribution of each individual tendency term along the way.

Trajectory sources for each box after back-propagating 30 min vary considerably depending on launch location (Fig. 12). The selected trajectory in Box A originates from above the storm (in the stratosphere) and does not appear to interact with the tilting and stretching of pre-existing $\boldsymbol{\omega}_h$ in the low- to midlevels at all (Fig. 13a). The first sign of rotation is the $\boldsymbol{\omega}_h$ generated baroclinically in the storm from ~70 to 75 min while the parcel is above 15 km (Fig. 14a). As the parcel crosses over the OT (denotated by the time at which the $\boldsymbol{\omega}_h$ components switch sign after $t = 75$ min) and is ingested into the storm (descending by >3 km), $> 0.1\ \mathrm{s}^{-1}$ of $\boldsymbol{\omega}_h$ is generated from the solenoidal term alone. The $\boldsymbol{\omega}_h$ generated is dampened by diffusion after ~77 min as the parcel is mixed into the storm. However, the remaining strong $\boldsymbol{\omega}_h$ is tilted into the vertical and enhanced by moderate convergence after $t = 80$ min. The parcel is above 12 km when the ζ is generated. Similar tendency terms and evolution are seen in Trajectory D (Figs. 13d and 14d), where tilting (and subsequent stretching) results in anticyclonic ζ. The ζ in both trajectories A and D within the AACP notably exhibit wavelike characteristics, with cyclonic and anticyclonic means, respectively, that appear out of phase with the horizontal divergence wave downstream of the OT. Positive stretching is particularly strong in the diverging segments of trajectories A and D, acting to dampen anticyclonic ζ in both. No vertical wind shear (no background $\boldsymbol{\omega}_h$) is present in the environment sounding above 6 km in this simulation, thus, the $\boldsymbol{\omega}_h$ at this height must be generated by the storm itself. It is worth noting here that, unlike the idealized numerical simulation, storms explored in section 4a do have negative vertical wind shear at the anvil-level, which may modulate the

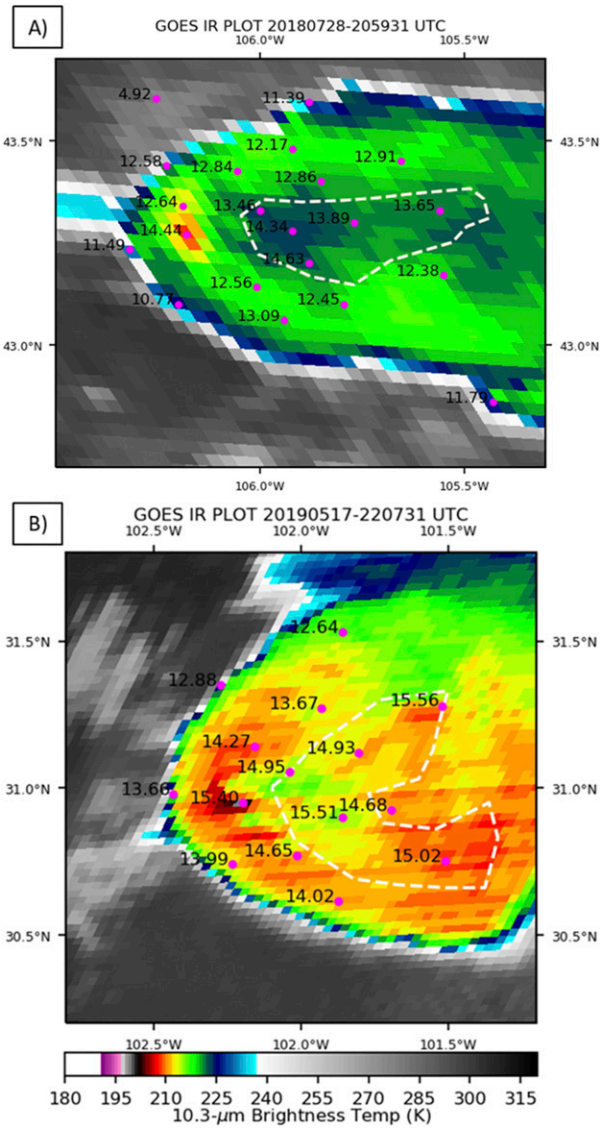

FIG. 7. (a) *GOES-16* 10.3-μm IR imagery for the 28 Jul 2018 case study and (b) *GOES-17* 10.3-μm imagery for the 17 May 2019 case study, each shown with AACP locations (white dashed line) and visible-derived stereoscopy CTH (pink dots and numbers; km).

strength and evolution of CTV from what is seen in Figs. 13 and 14. The current role of vertical wind shear in this explored CTVC formation process is unknown, and a likely subject of future sensitivity studies. Boxes A and D appear to be a mix of parcels from multiple altitudes, though most trajectories originate from the lower stratosphere as indicated by the average altitude line (black-dash). This conceptual view supports the Wang (2003) gravity-wave-breaking hypothesis, where moist convection air is detrained into the stratosphere above the storm.

Trajectory B originates from the low levels (<3 km; Fig. 13b), and acquires ζ by tilting of barotropic $\boldsymbol{\omega}_h$ (i.e., Weisman and Klemp 1982) as it ascends through the troposphere. Negative tilting and stretching terms (highlighted by

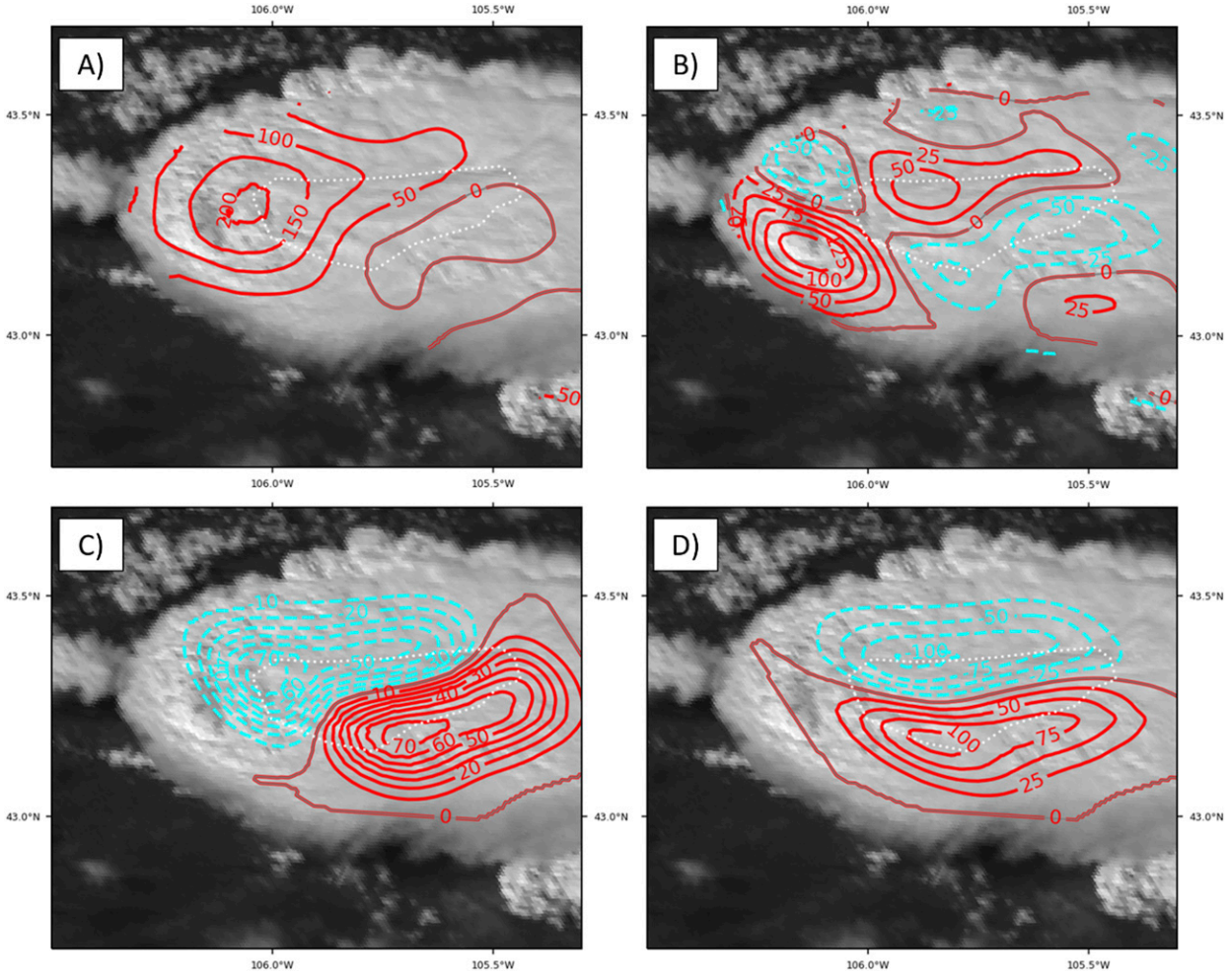

FIG. 8. The 2100 UTC 28 Jul 2018 supercell *GOES-16* 0.64-μm VIS imagery with (a) CTD contoured every $50 \times 10^{-5}\,s^{-1}$ and (b) CTV contoured every $25 \times 10^{-5}\,s^{-1}$ derived with vertical wind shear in the AACP mAMVs removed with positive (negative) values with red (cyan dashed). Also shown is the difference between the new fields in (a) and (b) and the original fields for (c) CTD and (d) CTV with CTD contoured every $10 \times 10^{-5}\,s^{-1}$ for clarity.

negative slopes in the integrated terms in Figs. 13b and 14b) above 7 km, however, reduce the ζ present in this parcel to near $0\,s^{-1}$ by $t = 87$ min. As the parcel approaches the storm-top, strong positive solenoidal ω_y generation occurs after $t = 84$ min above ~10 km (Fig. 14b). Dampening by diffusion can also be seen after $t = 88$ min. This $\boldsymbol{\omega}_h$ is then tilted into the vertical as the parcel ascends into the region downstream of the primary updraft. The horizontal convergence in this downstream region also contributes to strong cyclonic rotation.

Trajectory C, launched from the anticyclonic area immediately downstream of the OT, originates from the stratosphere, once again gaining ζ from baroclinically generated $\boldsymbol{\omega}_h$ (dampened by diffusion) that is tilted and converged downstream of the OT in a manner similar to trajectories A and D (Figs. 13c and 14c). The only trajectory samples that do have ζ near the cloud top generated by low-level tilting and subsequent stretching are those found in Box E (Figs. 13e and 14e). While positive ζ is found, which was generated from below 7 km, the magnitudes are only ~10% of what is found farther downstream of the OT.

Most of the parcels within Box C originate from lower levels, and many of these trajectories, like trajectory B, lose most of the ζ generated in the lower levels as they ascend toward the cloud top, and regain anticyclonic momentum from tilted $\boldsymbol{\omega}_h$ (e.g., Fig. 15). Additional trajectories for both Boxes B and C (purple lines in Figs. 13b,c) demonstrate this ζ trend, and further shows how parcels from the updraft experience the same strong solenoidal $\boldsymbol{\omega}_h$ generation as those which originate from the stratosphere downstream of the primary updraft (after 87 min in Figs. 15a,b). An analysis of the integrated ζ created by tilting and stretching through every trajectory explored in this study demonstrates how much is generated above 10 km versus how little originates from the levels below (Figs. 16a–e). Apart from the trajectories within the OT in Box E, ζ generated by tilting and stretching above 10 km in all trajectories is nearly one order of magnitude larger than what was

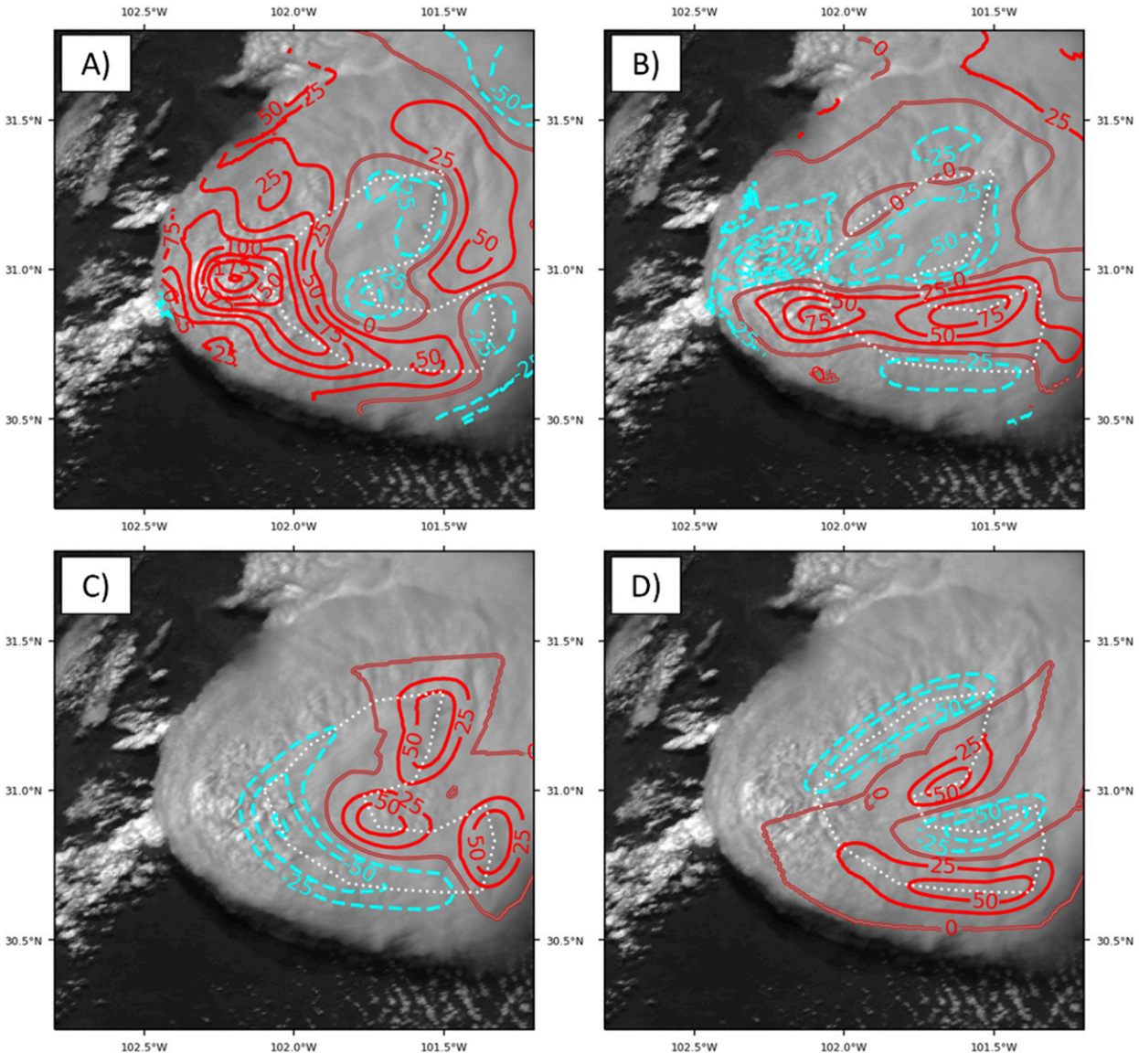

FIG. 9. As in Fig. 8, but for 2207 UTC 17 May 2019.

generated below 10 km (where the mesocyclone resides). Moreover, trajectories in the anticyclonic region (Figs. 16c,d) nearly all have cyclonic ζ generated from below 10 km, implying that the entirety of the anticyclonic ζ was generated well above the primary mesocyclone. Thus, the ζ observed downstream is largely determined not by what ζ is generated below 10 km in this WRF model simulation, but rather by what is generated near the OT above 10 km.

5. Discussion

Using advanced DOF derivation techniques, the common artifacts observed in CTD and CTV derivation from previous works (A16 and A18) are largely reduced. Uncertain transparency of the AACPs, however, prohibits the ability to resolve motion discontinuities mathematically that exist between the primary anvil and AACP. Enhanced CTV along the AACP edges observed in Fig. 4 without motion discontinuities in the raw DOF fields, in an environment with negative vertical wind shear above the anvil, implies that the DOF derivation approach found a mix of the two distinct motions. Background motion removal with image stereoscopy dampened the magnitude of the derived CTVCs; however, it did not remove its presence in either case study explored here. Therefore, the CTVCs shown in Figs. 8b and 9b are likely actual ζ present at the cloud top of the storm itself, and not an artifact of the derivation process. The background motion removal process was also an overestimate of the actual CTV enhancement caused by the vertical shear artifact, as evident by the many points in the AACP that were well below the highest altitude

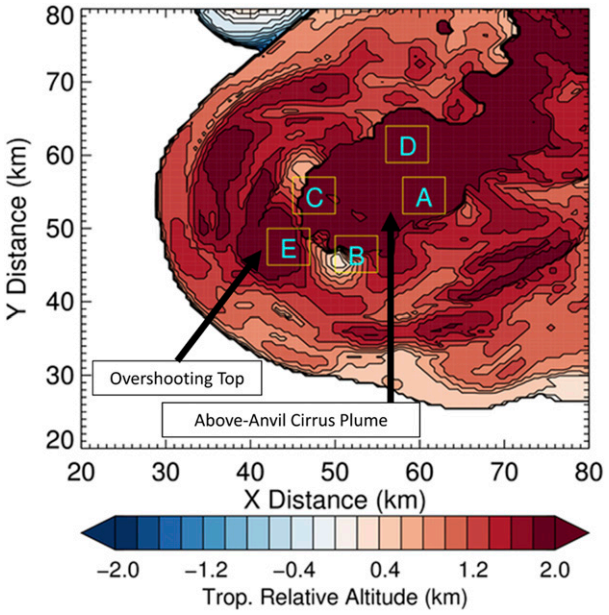

FIG. 10. The WRF-ARW idealized supercell CTH at 90 min relative to the tropopause at 12 km shown with initial trajectory locations for flow analysis. Each trajectory box contains a 10 × 10 grid of parcels to be tracked backward in time, whose bottom-left corners are defined in Table 2.

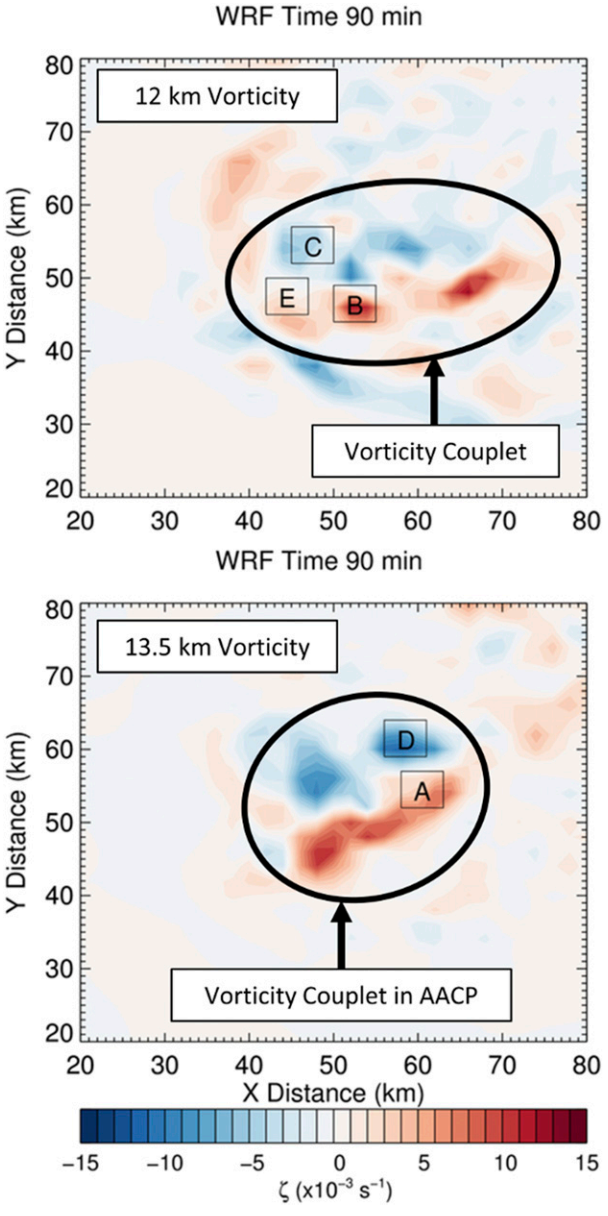

FIG. 11. The WRF-ARW vertical vorticity at 90 min at (top) 12 and (bottom) 13.5 km shown with initial trajectory box locations for flow analysis. Each trajectory box contains a 10 × 10 grid of parcels to be tracked backward in time, whose bottom-left corners are defined in Table 2. Vertical vorticity shown here was smoothed with averaging over 2 km × 2 km box kernels for clarity.

used to extract the background motion. It is also likely, in the cases of more transparent AACP cloud matter, that the DOF approach used here identified the motion below the AACP in the opaque cloud anvil.

While we find that these case studies appear to have CTV related to the actual ζ present at the top of the storm, the results also suggest that CTVCs can be mistakenly found in the presence of AACPs. If the AACP is opaque enough, and large negative vertical wind shear exists between the equilibrium level and the AACP altitude (typically 2–4 km above the primary anvil), then CTVCs can appear with the derivation process described above. It is therefore possible the vertical shear artifact may skew the severe storm identification and prediction results (that include CTV as a predictor) of larger statistical studies without a test for AACP edges and local vertical wind shear. Also, operational users may see an enhancement on VIS-imagery-derived flow products at sunset, where the presence of AACPs are highlighted in VIS imagery with more detailed shadowing (e.g., see Figs. 17a,b). Therefore, users should be skeptical of large CTV, which appears to exist along the edge of more prominent AACPs, which are quite common over significant severe DC (e.g., Bedka et al. 2018), and favor observations of CTV immediately downstream of the OT (if the viewing geometry and AACP transparency permit observations of the area). By removing the artifacts in the case studies here, the remaining ζ appeared to be in the area immediately downstream of the OT and was largely unaffected by the presence of the AACP.

From trajectory analysis, a new finding from this study is that the rotation observed at cloud top is likely not directly related to the main mesocyclone and anticyclone pair of the supercell where the ambient vertical wind shear layer is located (from 0–6 km), as hypothesized in A16. In fact, many trajectories with large ζ launched within the AACP do not even flow through the low- to midlevel structure (<10 km) of the simulated supercell storm. For the sake of illustration, the source of the CTVC identified in the model is shown as a schematic in Fig. 18a. While turbulence in the high-resolution model does cause differences in the exact tendencies from trajectory to

TABLE 2. Starting locations for backward trajectories in the bottom-left corner of each 10 × 10 pixel (5 km × 5 km) box in Fig. 10 beginning at 90 min in the WRF-ARW idealized simulation.

Trajectory	Starting X (km)	Starting Y (km)	Starting height (km AGL)
A	58	52	13.5
B	50	44	12
C	45	52	12
D	56	59	13.5
E	42	45	12

trajectory, many of the trajectories in the AACP and primary anvil shared the illustrated properties. Trajectories with positive (or negative) CTV in either the anvil or AACP first acquire positive ζ well downstream of the OT (within the WRF-ARW, above 13 km) through tilting of baroclinically generated $\boldsymbol{\omega}_h$. The baroclinic $\boldsymbol{\omega}_h$ generation is particularly strong immediately downstream of the OT, as is the dampening by the turbulent diffusion component. Hence, the parameterizations on the subgrid-scale processes can significantly regulate the overall quantity of ζ simulated in the WRF-ARW model. The ζ generated is then enhanced by stretching in strong convergence downstream of the initial baroclinic $\boldsymbol{\omega}_h$ generation.

Cross sections through the WRF-ARW output highlight key feature locations within the storm related to the processes described above. It is found that trajectories that experience strong baroclinic $\boldsymbol{\omega}_h$ generation in the upper levels (e.g., blue line in Figs. 19a,b) travel between the OT and the region with gravity wave breaking, where the isentropes bend upward yielding $\partial\theta/\partial z < 0\,\mathrm{K\,m^{-1}}$ (e.g., Wang 2003). The OT and the gravity wave breaking form a strong horizontal buoyancy gradient, demarcated with contours of the pressure gradient forces (purple arrows in Figs. 19c,d). While the trajectories suggest that the CTVC consists of a mix of parcels from the stratosphere and the storm, dry stratospheric air inhibits cloud formation necessary for the satellite detection. The CTVC likely then consists primarily of saturated parcels sourced from the storm (e.g., Fig. 15). The dry stratospheric air sinking into the storm through the gravity wave breaking region instead likely strengthens the buoyancy gradient by adding to the strong positive buoyancy downstream of the OT. The downward bending of the isentropes downstream of the OT, along with the baroclinic generation of $\boldsymbol{\omega}_h$ on the lee side of the OT, bears a close resemblance to the formation of lee ζ couplets

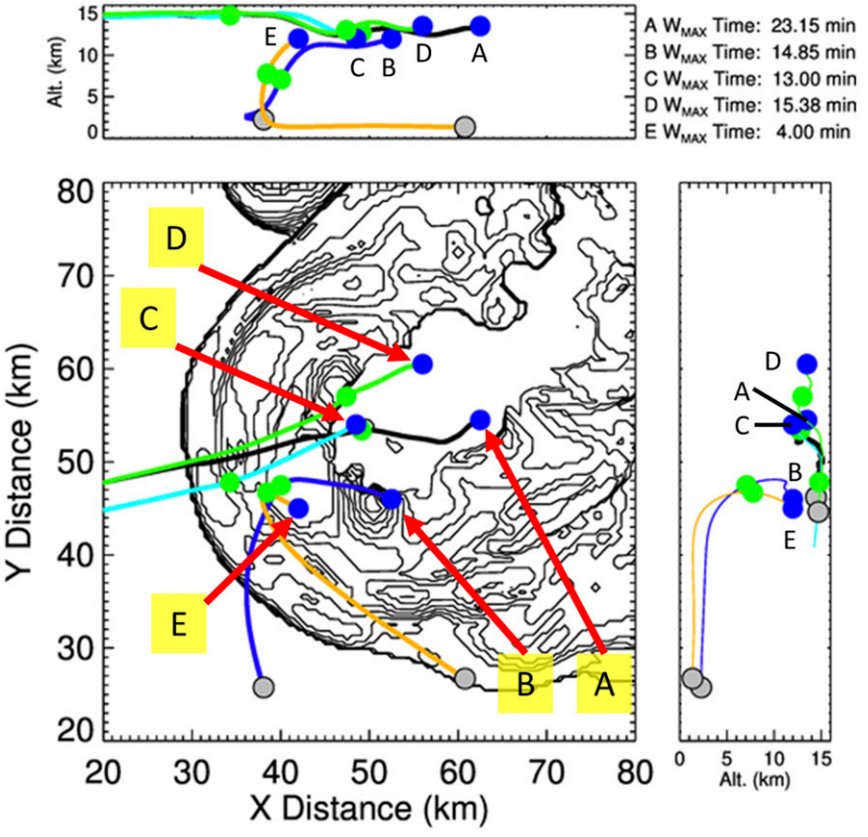

FIG. 12. The WRF-ARW idealized supercell cloud-top height at 75 min shown with trajectory starting (ending) locations marked with blue (gray) circles. Green circles indicate the location of the maximum w, and the relative time between the green and blue circles is shown on the top right for each trajectory.

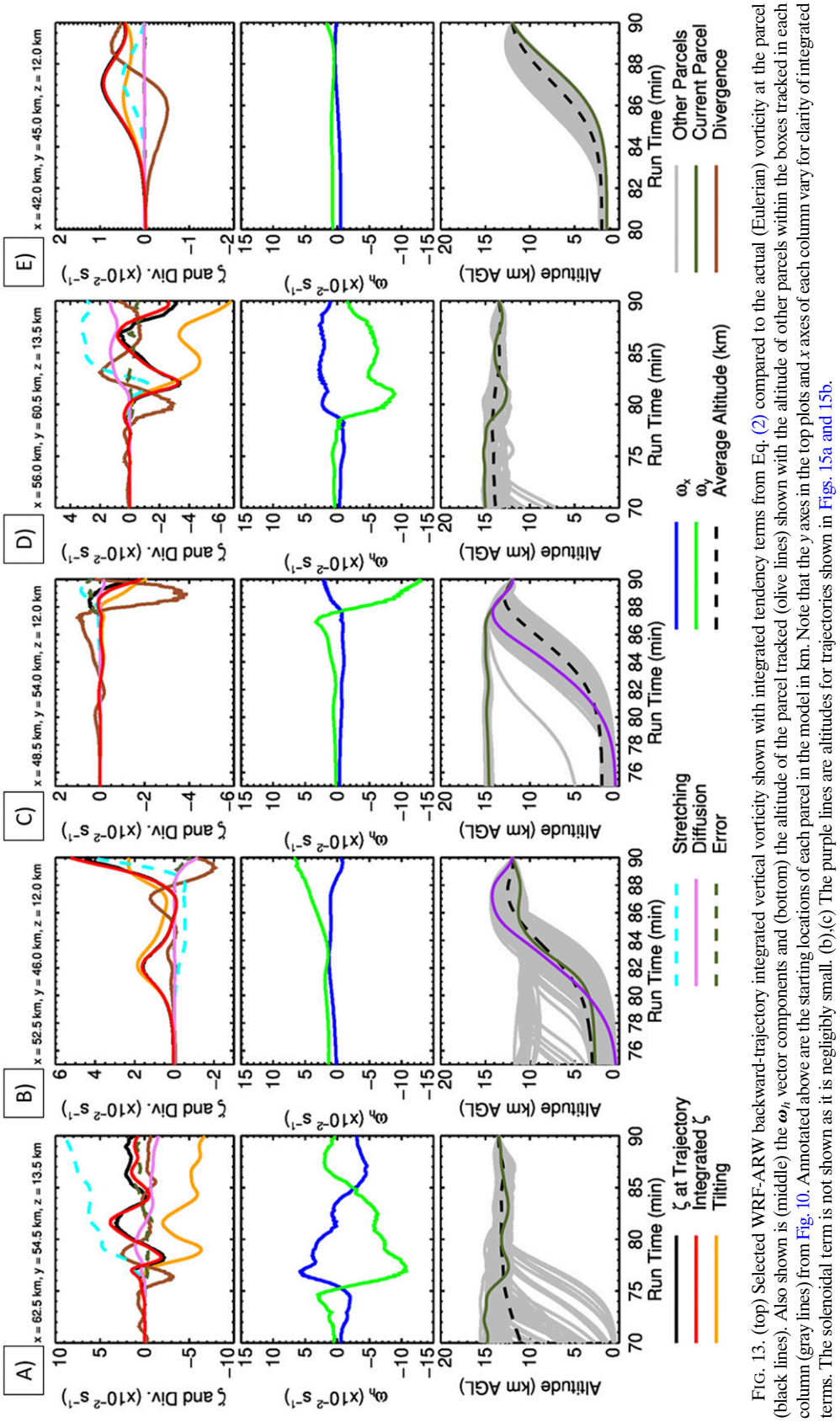

FIG. 13. (top) Selected WRF-ARW backward-trajectory integrated vertical vorticity shown with integrated tendency terms from Eq. (2) compared to the actual (Eulerian) vorticity at the parcel (black lines). Also shown is (middle) the $\boldsymbol{\omega}_h$ vector components and (bottom) the altitude of the parcel tracked (olive lines) shown with the altitude of other parcels within the boxes tracked in each column (gray lines) from Fig. 10. Annotated above are the starting locations of each parcel in the model in km. Note that the y axes in the top plots and x axes of each column vary for clarity of integrated terms. The solenoidal term is not shown as it is negligibly small. (b),(c) The purple lines are altitudes for trajectories shown in Figs. 15a and 15b.

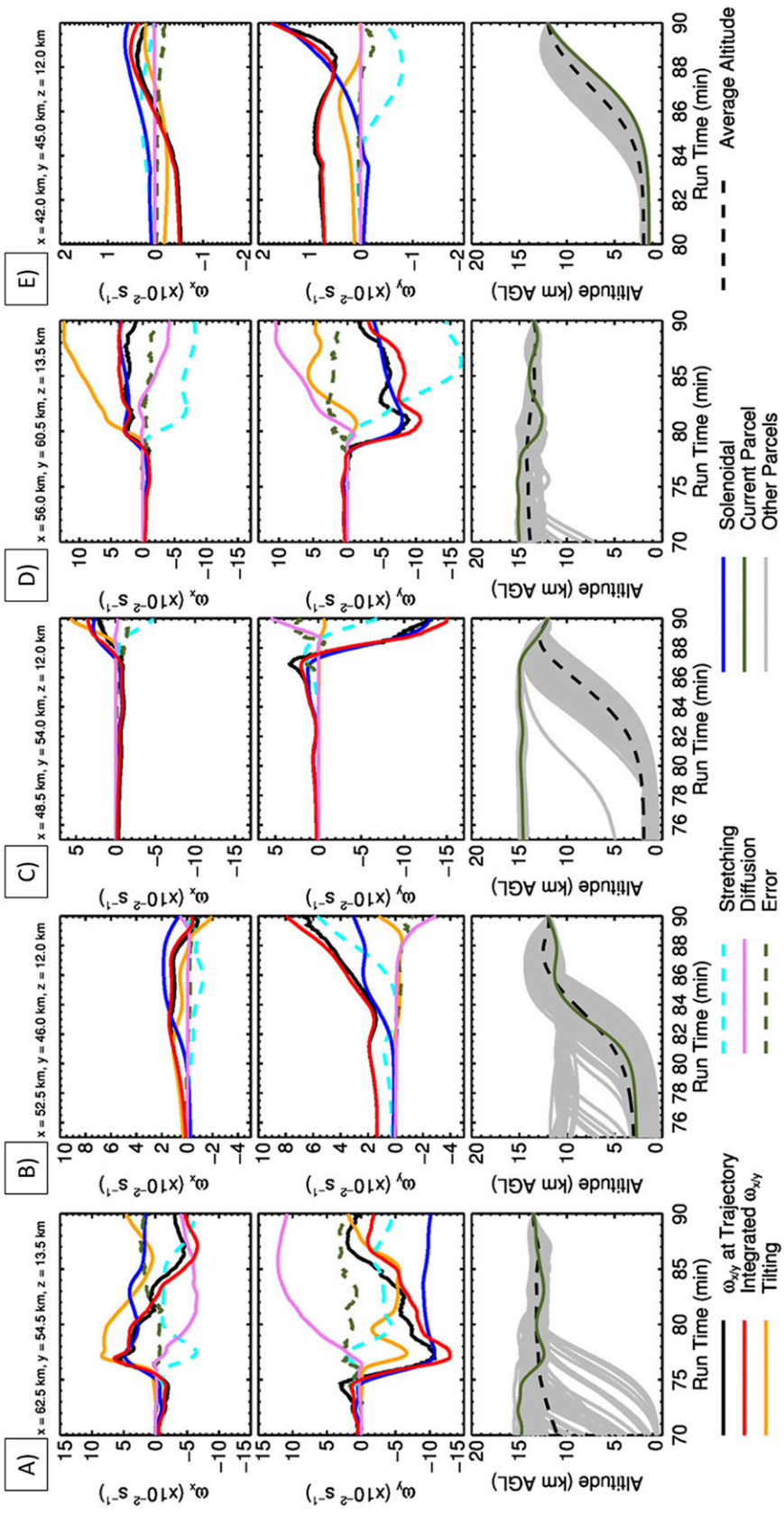

FIG. 14. (top),(middle) Selected WRF-ARW backward-trajectory integrated $\boldsymbol{\omega}_i$ (ω_x and ω_y) shown with integrated tendency terms from Eq. (2) compared to the actual (Eulerian) vorticity at the parcel (black lines) for the same parcels shown in Fig. 13. (bottom) Also shown for reference are the same parcel altitudes from Fig. 13. Note that the x and y axes of each column vary for clarity of integrated terms.

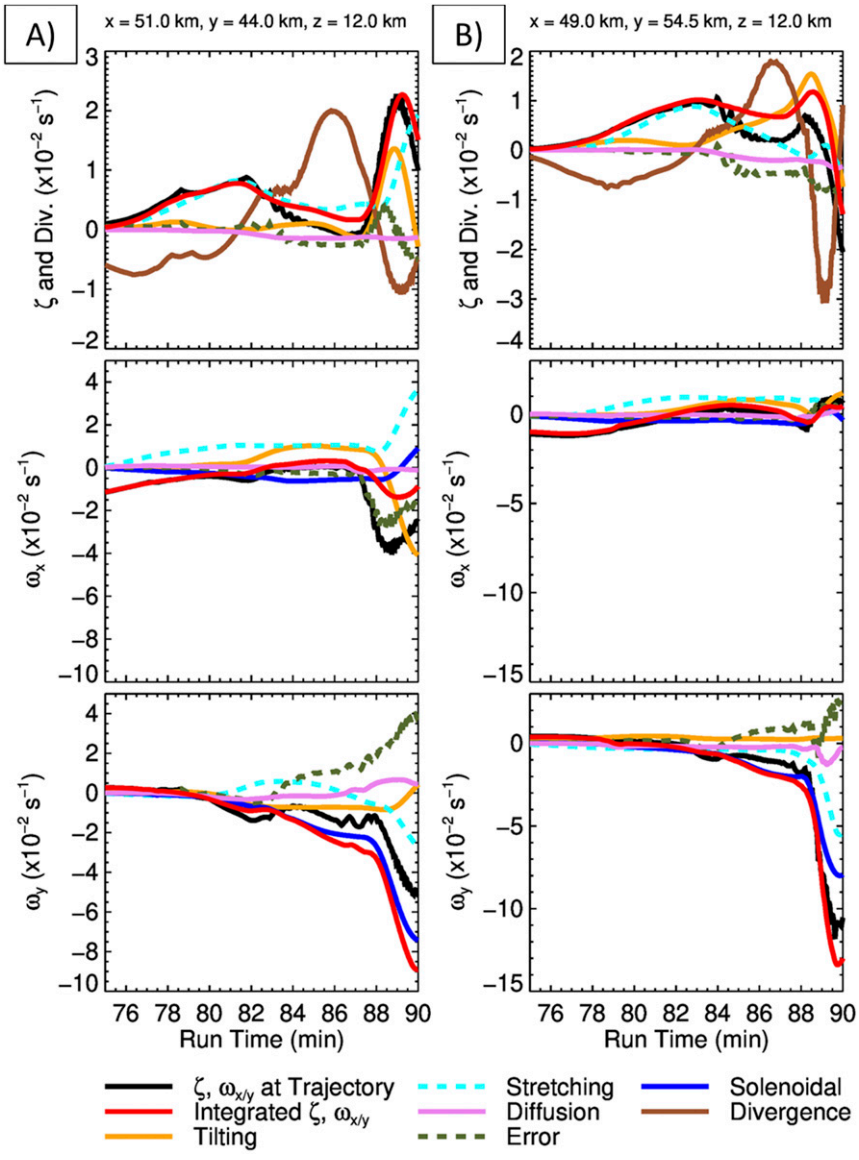

FIG. 15. Selected WRF-ARW backward-trajectory integrated (top) ζ, (middle) ω_x, and (bottom) ω_y for the purple trajectories from (a) box B shown in Fig. 13b (bottom) and (b) box C shown in Fig. 13c (bottom) shown with integrated tendency terms from Eq. (8) compared to the actual (Eulerian) vorticity at the parcel (black lines). Annotated above are the starting locations of each parcel in the model in km.

downstream of flow over mountains and bluffs as described in Smolarkiewicz and Rotunno (1989).

The negative buoyancy within the OT, and the positive buoyancy lower in the storm, also contributes to moderate $\boldsymbol{\omega}_h$ generation as parcels ascend through the updraft (cyan arrow). For parcels that remain beneath the OT, strong $\boldsymbol{\omega}_h$ can be baroclinically generated as parcels move downstream of the positive buoyancy sector (e.g., orange line and green arrow in Figs. 19c,d; Trajectory B in Fig. 13b). These parcels generate large ζ (again above the tilting and stretching related to the lower mesocyclone), though likely exist beneath the cloud top as evident from the $\omega_y < 0$, which implies that the horizontal velocity maximum within the cloud is above the parcel of interest (contrast with the $\omega_y > 0$ for parcels that are lofted higher into the storm; e.g., Figs. 15a,b). We further include a schematic to reflect on these baroclinic generation mechanisms and how they relate to CTV, which is shown in Fig. 20.

Trajectories originating below 10 km have rotation consistent with the Rotunno and Klemp (1982) tilting and stretching mechanisms once they reached the OT. However, additional tilting and stretching takes place after the parcels subside downstream of the OT. It is possible that some of the cyclonic ζ reaches the cloud top from the low- to midlevels, implied by trajectories in Box E, though the magnitude in the WRF-ARW

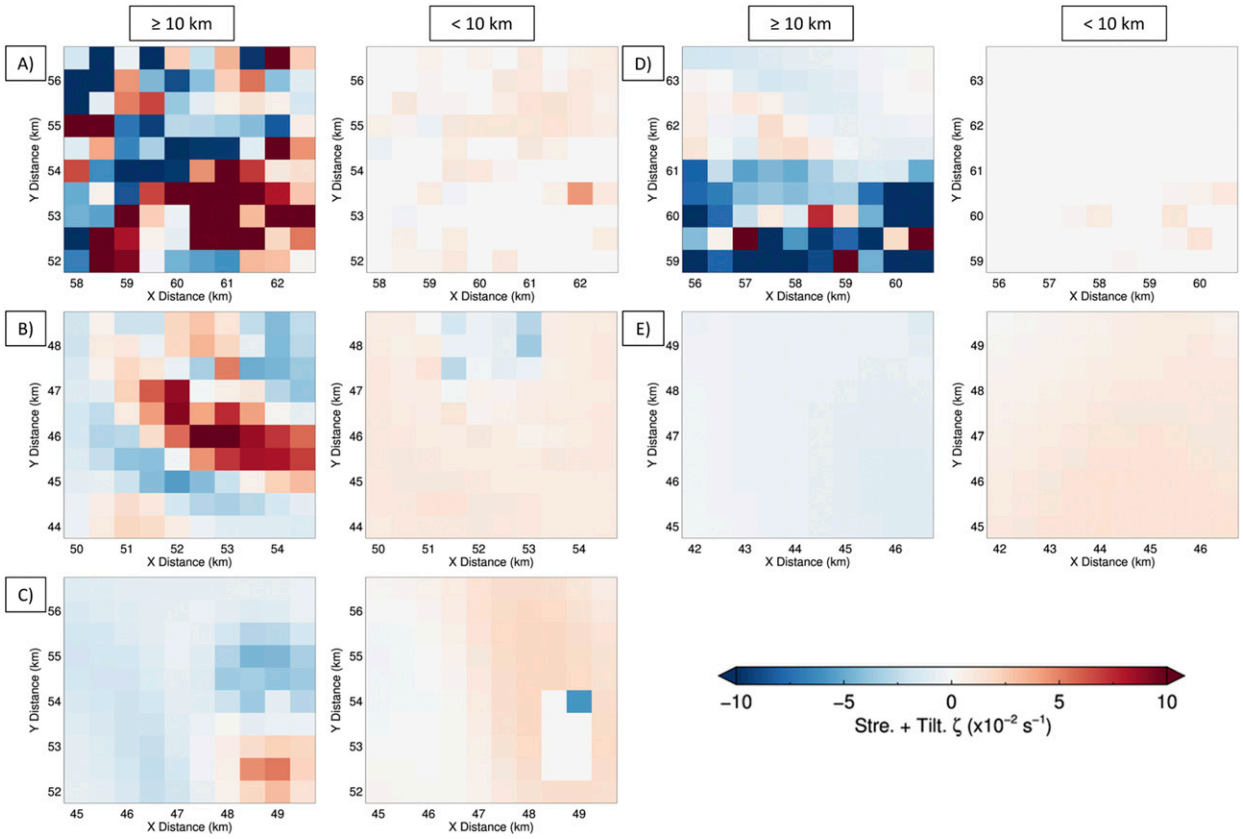

FIG. 16. The WRF-ARW integrated vertical vorticity caused by tilting and stretching at altitudes (left) ≥10 and (right) <10 km through all trajectories tracked in boxes A through E.

simulation is considerably smaller than what is generated in the upper levels of the storm (as in Fig. 15), and not likely resolved by the objective DOF analysis used here. A separate schematic illustrates where the ζ generated below midlevels (~7 km in this simulation) is hypothesized to be located at cloud top based on the model, if it can even be observed, compared to the ζ generated in the upper levels (above ~10 km; Fig. 18b). We note that the CTVC signature was only found over severe DC in A16. The results here suggest that the strength and persistence of the updraft (required for strong and persistent baroclinic $\boldsymbol{\omega}_h$ generation by the storm and gravity wave breaking between the stratosphere and the storm), rather than the midlevel rotation, is what is responsible for the formation of the CTVC (similar to how the updraft strength and persistence is related to the formation of the AACP; Wang 2003; Homeyer et al. 2017; Bedka et al. 2018).

A few errors may have impacted the trajectory analysis here. As discussed in Dahl et al. (2012), trajectories are sensitive to the selection of gridpoint spacing and integration time step. This sensitivity is dependent on the characteristics of the flow and backward trajectories may be susceptible to displacement error within a broadly rotating and confluent area in the mixing stage of the storm and the lower stratosphere. This error is mitigated here with 1-s WRF-ARW Model history file output and 0.5-s integration. Furthermore, the gradients used here were derived using simple trilinear interpolation, which, in highly turbulent and nonlinear flow, may not be adequate representations of the actual tilting and stretching terms. These discretization assumptions likely result in part of the inaccuracies observed between the computed total ζ and the actual ζ (the "error" term in Figs. 13–15), and likely why we found parcels sourced from the dry and sinking stratospheric air within the saturated storm cloud tops. For both errors, finer-resolution models can mitigate issues in future works.

Human matching errors aside, fast cloud motions and image distortions between *GOES-16* and *GOES-17* images may have caused inaccuracies in the stereoscopy analysis used to estimate the magnitude of the vertical shear artifact. Typical movements in clouds between frames of near-geosynchronous scans only result in ~0.5-km CTH errors here, though differences in incoming VIS radiation from different viewing angles, and feature distortion from different viewing angles, could cause larger CTH approximation errors. Improved stereoscopy, perhaps with a low-Earth-orbiting imagers, coupled with further WRF-ARW experiments with sheared layers, will further elucidate the vertical wind shear artifact's impact on traditional cloud-top flow-field derivation products.

6. Conclusions

The origin of CTVC signatures over severe thunderstorms derived objectively using DOF vectors on 1-min GOES-R-era

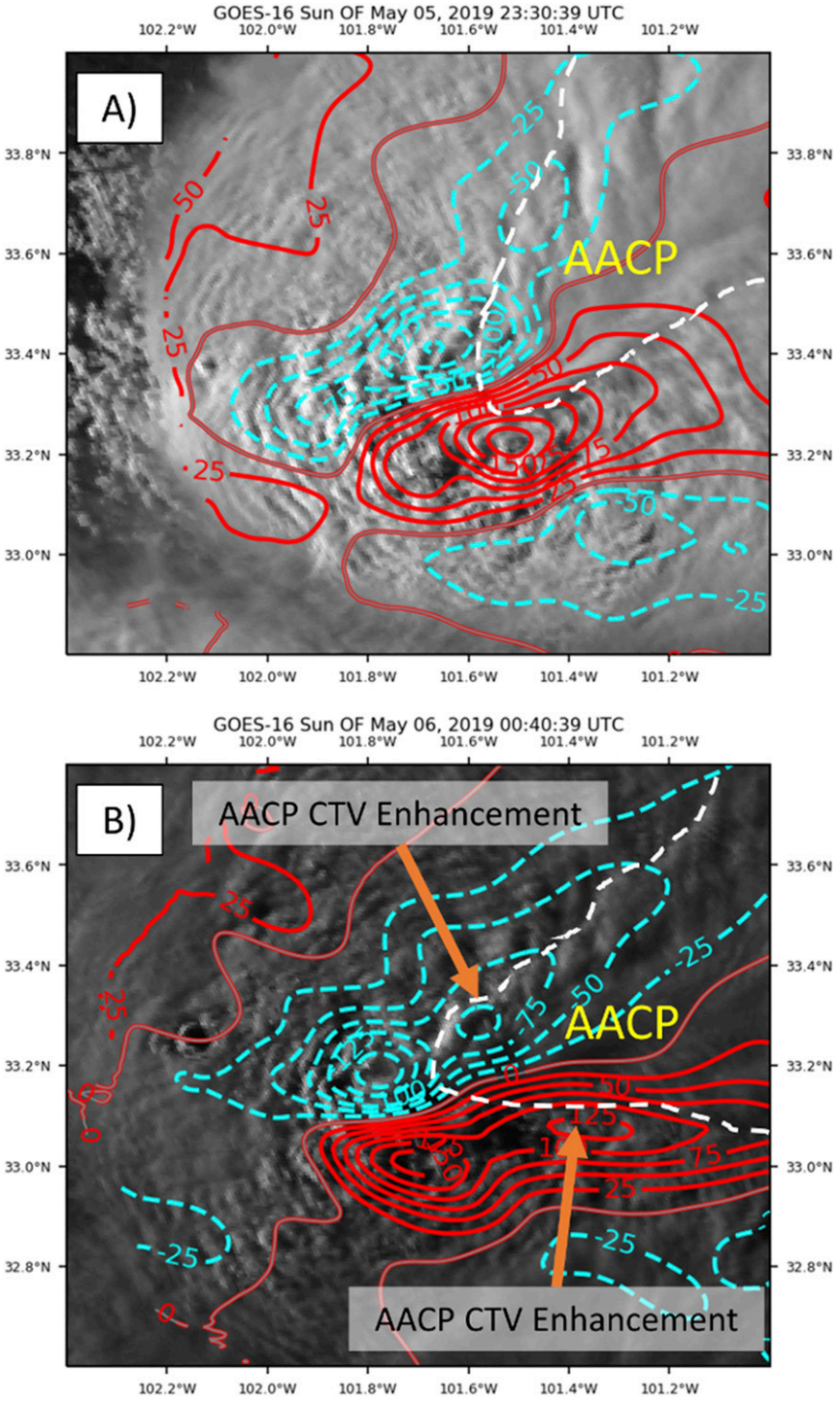

FIG. 17. Example *GOES-16* VIS imagery and CTV derived using the method outlined in section 3a contoured with positive (negative) values every $25 \times 10^{-5}\,s^{-1}$ in red (cyan dashed), showing a prominent AACP and the CTV enhancement that occurs as the sun sets over central TX at (a) 2330 UTC 5 May and (b) 0040 UTC 6 May 2019. The AACP is highlighted by the region within the white dashed lines in (a) and (b).

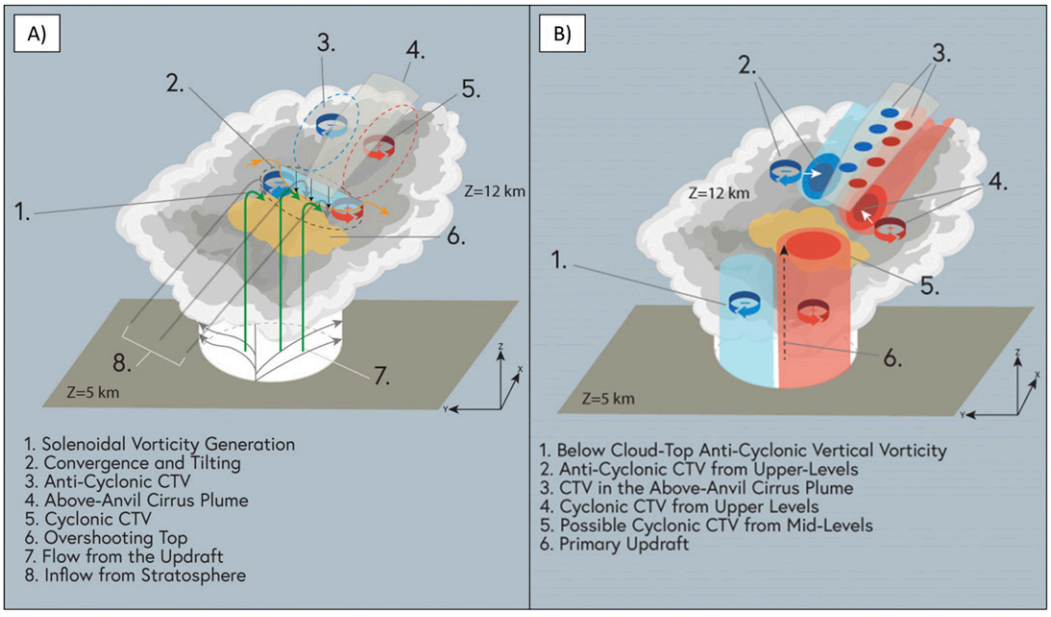

FIG. 18. (a) Schematic of the vortex line (shown in orange) within a supercell downstream of the inflow from the primary updraft (green arrows) and dry stratospheric air (gray arrows). Blue shading implies downward displacement of vortex lines. The dashed black ellipse represents the area of convergence and stretching enhancement that forms the CTVC observed with 1-min GOES imagery over strong DC (dashed red and blue ellipses). (b) Schematic of hypothesized vertical vorticity regions within and atop the supercell and AACP as identified by the numerical model used in this study.

imagery is explored here. Mechanisms that would generate "actual" versus "apparent" CTV signatures are both examined using case studies and a numerical model simulation. The primary findings are as follows:

- Using a motion-discontinuity-preserving DOF algorithm, manual AACP identification, numerical model environmental wind approximations, and image stereoscopy to remove anvil-edge and multi-cloud-layer vertical-shear-related flow-field artifacts, it is demonstrated that the CTVCs derived in the 28 July 2018 and 17 May 2019 case study supercells are indeed caused by actual rotation within the storm anvils. The demonstration here suggests that actual CTV can be observed by GOES-R-era 1-min VIS imagery if the viewing geometry and AACP transparency allow for the observation of the region immediately downstream of the OT (which was the case in the case studies by A16 and A18).
- CTV (and CTVCs) derived with 1-min GOES VIS imagery were originally thought to be related to the formation of cyclonic and anticyclonic vertical vorticity below 10 km within a supercell. Instead, using backward trajectories from cyclonic and anticyclonic CTV in an idealized supercell simulation, it is found that CTV primarily originates from horizontal vorticity that is baroclinically generated by the storm in the upper levels (>10 km) in a buoyancy gradient between the primary OT and the gravity-wave-breaking sector. The horizontal vorticity is tilted into the vertical and enhanced by convergence downstream of the primary OT. While vertical vorticity associated with tilting and stretching of vertical wind shear below 10 km was found within the OT, this vertical vorticity was an order of magnitude less than what is generated in the upper levels, and is lost with time as the parcels flow through an environment with strong divergence and unfavorable tilting above the updraft maximum in the WRF-ARW simulation.
- Removal of the maximum possible CTV caused by the vertical shear artifact reduced both cyclonic and anticyclonic CTV near the streamwise-parallel edges of the AACP and had negligible impact on CTV that was observed immediately downstream of the OT in the case studies examined here. The downstream CTV removed was large enough (~80% of the peak CTV magnitudes) to suggest that CTVCs can be artifacts of top-down observation if the AACPs are opaque enough and the negative vertical wind shear above the anvil is high. AACPs were also found to reduce CTD near the OT, though the magnitude change was smaller than the reduction to CTV.

The conclusions above address the two primary questions posed in the introduction (section 1), though another question looms for future studies to answer: How do we reduce the impact of artifacts on DC cloud-top flow-field derivation methods when present? The advanced DOF method developed by the computer vision community significantly reduced the common anvil-edge artifacts observed when simply using an objective analysis on sparse mAMV data. However, new DOF techniques will be required to address cases when transparent AACPs are present, where traditional variational DOF techniques (and operational AMV techniques) may mix derivable motions, as was observed in this study. As AACPs

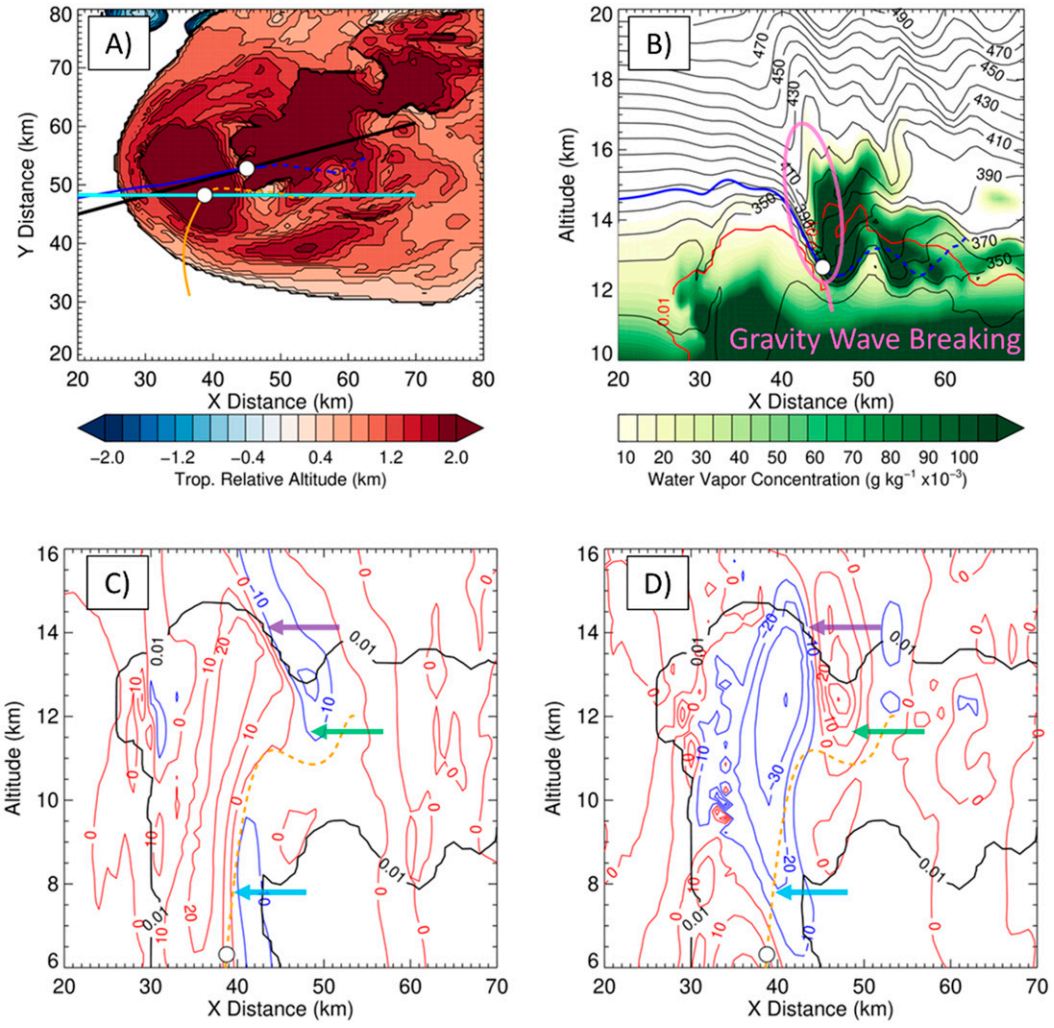

FIG. 19. (a) The WRF-ARW idealized supercell CTH relative to the tropopause at 12 km at 76 min 40 s shown with trajectory A from Figs. 13 and 14 (blue line/white dotted) and a trajectory from box B (initiated from x = 53.5 km, y = 48 km; orange line/white dotted). Each trajectory is shown such that previous (future) times are shown with a solid (dashed) line. (b) The cross section taken from the black line in (a) showing potential temperature contours every 10 K (black contours), water vapor concentration (color shaded contours; g kg^{-1} × 10^{-3}), the cloud water mixing ratio 0.01 g kg^{-1} contour (red line), and trajectory A (blue line). Also shown is another cross section taken at the cyan line in (a) of the pressure gradient force in (c) the x direction and (d) the z direction with positive (negative) values contoured in red (blue) every 10 × 10^{-2} m s^{-2}, with a trajectory from box B shown in orange. The arrows highlight key gradients in pressure gradient force that result in solenoidal $\boldsymbol{\omega}_h$ generation (see main text).

will almost always be present when CTVCs are observable (as they typically are for severe, rotating thunderstorms as found in Bedka et al. 2018), it would likely be helpful to couple the flow-field product here with both an automated stereoscopy approach (which handles the complex computer vision-related issues discussed in appendix B) and an objective AACP identification system once developed. Such a coupling can enable accurate objective DOF field quality control and adjustments, as was done subjectively in section 4a, for real-time products and operational analysis.

Another unanswered question here is how the strength of the updraft and other environmental features impact observable CTV? CTVCs have only been observed over supercell thunderstorms, which imply that, like AACPs and enhanced-V signatures, a strong and sustained updraft is required for the feature to exist. The direct relationship between updraft strength, low-level, and upper-level vertical wind shear, as well as upper-level thermodynamics, can be explored with further high-resolution numerical modeling studies. Of note is the fact that the case studies observed here generated CTVCs where negative vertical wind shear exists, which was not simulated and could modulate the magnitudes and formation mechanisms found here. Further investigation into the environmental impacts on the generation of CTV may yield

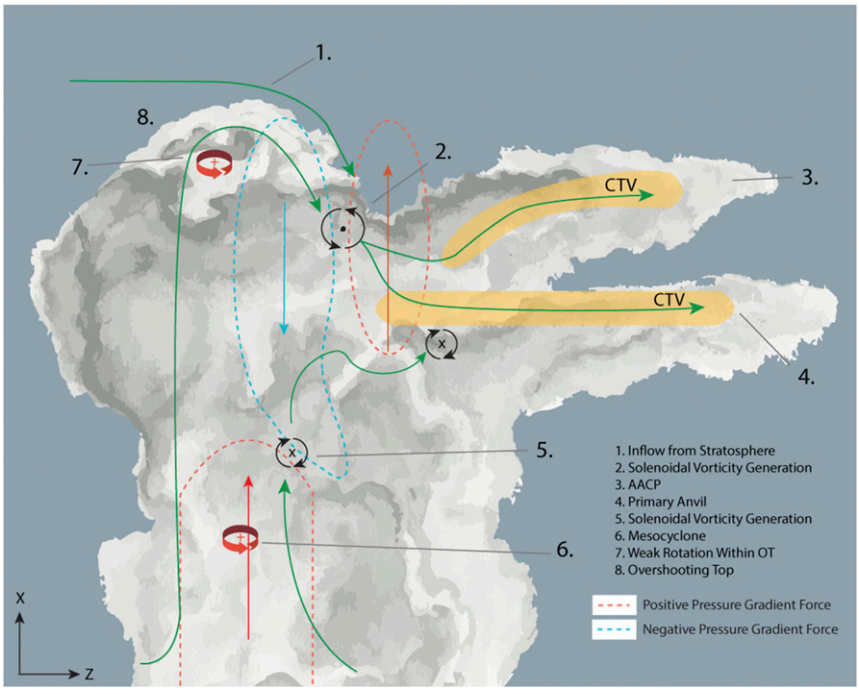

FIG. 20. (a) Schematic of locations of solenoidal $\boldsymbol{\omega}_h$ generation from a side view of the supercell storm for air flowing from the primary updraft and air mixing in from the stratosphere (green arrows). Red (blue) dashed shapes and arrows indicate regions with positive (negative) vertical pressure gradient force.

more clues into how to use the CTVCs to diagnose storm severity potential.

Acknowledgments. This work was funded by NSF Grants AGS-1261368 and AGS-1746119, NASA Grant NNX15AV82G, and the NESDIS GOES-R Program Office Award NA14OAR4320125. The authors thank the many researchers who provided invaluable feedback on the flow-field and vorticity analysis presented here, including Dr. Louie Grasso at the Cooperative Institute for Research in the Atmosphere, Dr. Cameron Homeyer at the University of Oklahoma School of Meteorology, and Drs. Lawrence Carey, Kevin Knupp, and Eugene McCaul, Jr., from the Department of Atmospheric Science at the University of Alabama in Huntsville. We would also like to thank Jennifer Geary from the University of Alabama in Huntsville for her graphic artistry work on the schematics in Figs. 18 and 20. Finally, we wish thank editor Dr. Christopher Weiss and the three anonymous reviewers who helped improve this study.

Data availability statement. GOES-R satellite imagery used for optical flow computation is publicly available via the National Oceanic and Atmospheric Administration Comprehensive Large Array-Data Stewardship System (NOAA-CLASS; http://www.class.noaa.gov). The WRF-ARW model is also available as open-source code via the WRF Users Page (https://www2.mmm.ucar.edu/wrf/users/downloads.html). Additional data can be provided upon request to the corresponding author.

APPENDIX A

Optical Flow Derivation Technique

Following the Sun et al. (2014) technique, we solve for DOF $\mathbf{U} = [u, v]^{\mathrm{T}}$ at every image pixel $\mathbf{x} = [x, y]^{\mathrm{T}}$ over the entire image by optimizing the energy E, defined as

$$E(u,v) = \sum_{i,j}[\rho_d(\mathrm{BC}_{i,j} + \gamma\,\mathrm{GC}_{i,j}) + \alpha\,\rho_s(\mathrm{SC}_{i,j})] + \lambda_c C + \lambda_n M. \tag{A1}$$

Equation (A1) variationally penalizes OF estimate deviations from assumptions of brightness constancy (BC), gradient constancy (GC), and the smoothness constraint (SC of the flow, and applies a weighted median smoothing filter M to the flow field, which is coupled to the solution with term C. The penalizations are weighted by constants γ, α, λ_c, and λ_n. The robust data ρ_d and smoothness ρ_s functions encompass penalizations in order to preserve motion discontinuities in the possible solutions for $\mathbf{U}$ (Black and Anandan 1996). The Charbonnier function is used:

$$\rho_d(r^2) = \rho_s(r^2) = \sqrt{r^2 + \epsilon^2}, \tag{A2}$$

where $\epsilon = 0.001$ is present to keep Eq. (A1) differentiable when $r^2 = 0$. Following Brox et al. (2004), the penalizations are mathematically defined as

TABLE A1. Settings used in the Sun et al. (2014) optical flow scheme.

Parameter	Value
Coarse-to-fine pyramid levels	4
Warping iterations (l)	3
Heuristic median filter iterations	5
Pyramid scale factor (SF)	0.5
γ	2
α	50
$\rho_d(x)$	$\sqrt{x+\epsilon}$
$\rho_s(x)$	$\sqrt{x+\epsilon}$
ε	0.001
λ_n	1

$$\begin{aligned} \mathrm{BC}_{i,j} &= |I(\mathbf{x}_{i,j}+\mathbf{U}_{i,j}, t+\Delta t) - I(\mathbf{x}_{i,j}, t)|^2, \\ \mathrm{GC}_{i,j} &= |\nabla I(\mathbf{x}_{i,j}+\mathbf{U}_{i,j}, t+\Delta t) - \nabla I(\mathbf{x}_{i,j}, t)|^2, \\ \mathrm{SC}_{i,j} &= |\nabla u_{i,j}|^2 + |\nabla v_{i,j}|^2, \end{aligned} \tag{A3}$$

where I is the image brightness and ∇ is the horizontal gradient operator. The coupling and median smoothing terms are defined as

$$\begin{aligned} C &= \|\mathbf{u}-\hat{\mathbf{u}}\|^2 + \|\mathbf{v}-\hat{\mathbf{v}}\|^2, \\ M &= \sum_{i,j}\sum_{(i',j')\in N_{i,j}} w_{i,j}^{i',j'}(|\hat{u}_{i,j}-\hat{u}_{i',j'}| + |\hat{v}_{ij}-\hat{v}_{i',j'}|), \end{aligned} \tag{A4}$$

where $\hat{\mathbf{u}}$ and $\hat{\mathbf{v}}$ represent an auxiliary, weighted median smoothed flow field. The median smoothing is weighted by horizontal distance and IR T_b difference, where

$$w_{i,j}^{i',j'} = \exp\left\{-\frac{|i-i'|^2+|j-j'|^2}{2\sigma_1^2} - \frac{|T_{b_{i,j}} - T_{b_{i',j'}}|^2}{2\sigma_2^2}\right\}. \tag{A5}$$

The filter-weight constants σ_1 and σ_2 are then set to 3 pixels and 20 K, respectively. This bilateral weighting is used internally in the raw DOF derivation and should not be confused with the separate postprocessing smoothing used in Eq. (1). The T_b used is the 10.35-μm IR "window" channel, scaled to the ~500-m *GOES-16* or *GOES-17* VIS resolution with bilinear interpolation. We follow Eq. (12) from Brox et al. (2004) to set up Eq. (A1) as a sparse linear system of equations, using the discretization from Brox (2005) for the divergence of the robust smoothness constraint.

The discrete linear system of equations is minimized following the alternating minimization approach described in Sun et al. (2014). At each alternating step, the sparse linear system of equations is solved with a graphics processing unit accelerated conjugate gradient algorithm (e.g., Sundaram et al. 2010). A coarse-to-fine optimization scheme is used here, with specific settings outlined in Table A1. The image pyramid is set to be deep enough such that no reasonable motions exceed one pixel at each level. At every pyramid level, the coupling weight λ_c is increased logarithmically from 1×10^{-4} to 100 at each warping iteration l. The VIS images input into the DOF scheme are set at the raw (maximum) radiometric resolution for maximum detail in spatial and temporal intensity gradients and normalized to floating point values between 0 and 255.

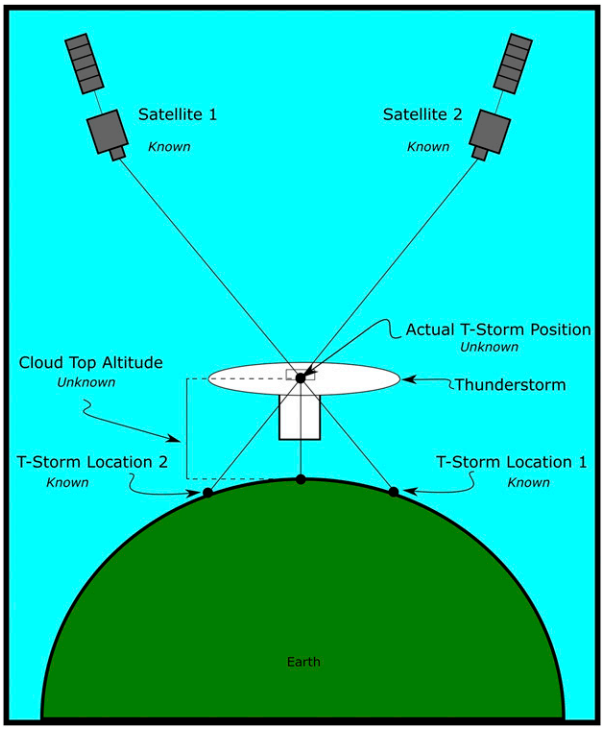

FIG. B1. Schematic of image stereoscopy with two satellites used to derive the cloud-top altitude of a thunderstorm.

APPENDIX B

Image Stereoscopy

Image stereoscopy is used to assess the height of each cloud-layer (primary anvil and AACP) without the typical drawback of T_b and NWP model-height assignment in inversions, as present in the lower stratosphere (e.g., Heidinger 2013). The image stereoscopy method used here follows previous works on the subject (Hasler 1981; Hasler et al. 1991; Wylie et al. 1998). The overlapping CONUS images from the complementary satellite within 30 s of the mesoscale sector image (at scan time) are remapped to the image projection of the mesoscale sector with bilinear interpolation. The VIS imagery brightness between the two satellites is normalized at each time frame for better feature matching. Image pixels from each satellite are then corresponded together by a human expert. Manual target correspondence avoids typical issues in automated approaches based on patch-matching with cross-correlation (e.g., Hasler et al. 1991; Carr et al. 2018). For example, much like the AMVs described in section 2a, the assumptions within automated patch-matching approaches for image stereoscopy break down where multiple correspondence solutions exist within a single target (e.g., between multiple cloud layers and within transparent cloud scenes). The CTH of corresponded targets are then determined using trigonometry

(Fig. B1). Due to both the pixelated granularity of the satellite imagery and imperfections in the correspondence of exact locations for targets in *GOES-16* and *GOES-17*, lines subtended between imagers and targets seldom intersect. The inferred CTH is thus derived by identifying a midpoint between the two nearest points in each subtended line, which is inferred as the actual three-dimensional location.

REFERENCES

Adlerman, E. J., K. K. Droegemeier, and R. Davies-Jones, 1999: A numerical simulation of cyclic mesocyclogenesis. *J. Atmos. Sci.*, **56**, 2045–2069, https://doi.org/10.1175/1520-0469(1999)056<2045:ANSOCM>2.0.CO;2.

Apke, J. M., J. R. Mecikalski, and C. P. Jewett, 2016: Analysis of mesoscale atmospheric flows above mature deep convection using super rapid scan geostationary satellite data. *J. Appl. Meteor. Climatol.*, **55**, 1859–1887, https://doi.org/10.1175/JAMC-D-15-0253.1.

——, ——, K. M. Bedka, E. W. McCaul Jr., C. R. Homeyer, and C. P. Jewett, 2018: Relationships between deep convection updraft characteristics and satellite based super rapid scan mesoscale atmospheric motion vector derived flow. *Mon. Wea. Rev.*, **146**, 3461–3480, https://doi.org/10.1175/MWR-D-18-0119.1.

Baker, S., D. Scharstein, J. P. Lewis, S. Roth, M. J. Black, and R. Szeliski, 2011: A database and evaluation methodology for optical flow. *Int. J. Comput. Vis.*, **92**, 1–31, https://doi.org/10.1007/s11263-010-0390-2.

Barron, J. L., D. J. Fleet, and S. S. Beauchemin, 1994: Performance of optical flow techniques. *Int. J. Comput. Vis.*, **12**, 43–77, https://doi.org/10.1007/BF01420984.

Bedka, K. M., and J. R. Mecikalski, 2005: Application of satellite-derived atmospheric motion vectors for estimating mesoscale flows. *J. Appl. Meteor.*, **44**, 1761–1772, https://doi.org/10.1175/JAM2264.1.

——, and K. Khlopenkov, 2016: A probabilistic multispectral pattern recognition method for detection of overshooting cloud tops using passive satellite imager observations. *J. Appl. Meteor. Climatol.*, **55**, 1983–2005, https://doi.org/10.1175/JAMC-D-15-0249.1.

——, J. Brunner, R. Dworak, W. Feltz, J. Otkin, and T. Greenwald, 2010: Objective satellite-based detection of overshooting tops using infrared window channel brightness temperature gradients. *J. Appl. Meteor. Climatol.*, **49**, 181–202, https://doi.org/10.1175/2009JAMC2286.1.

——, C. Wang, R. Rogers, L. D. Carey, W. Feltz, and J. Kanak, 2015: Examining deep convective cloud evolution using total lightning, WSR-88D, and *GOES-14* super rapid scan datasets. *Wea. Forecasting*, **30**, 571–590, https://doi.org/10.1175/WAF-D-14-00062.1.

——, E. Murillo, C. R. Homeyer, B. Scarino, and H. Mersiovski, 2018: The above-anvil cirrus plume: An important severe weather indicator in visible and infrared satellite imagery. *J. Appl. Meteor. Climatol.*, **33**, 1159–1181, https://doi.org/10.1175/WAF-D-18-0040.1.

Benjamin, S. G., and Coauthors, 2016: A North American hourly assimilation and model forecast cycle: The Rapid Refresh. *Mon. Wea. Rev.*, **144**, 1669–1694, https://doi.org/10.1175/MWR-D-15-0242.1.

Betten, D. P., M. I. Biggerstaff, and L. J. Wicker, 2017: A trajectory mapping technique for the visualization and analysis of three-dimensional flow in supercell storms. *J. Atmos. Oceanic Technol.*, **34**, 33–49, https://doi.org/10.1175/JTECH-D-16-0043.1.

Black, M. J., and P. Anandan, 1996: The robust estimation of multiple motions: Parametric and piecewise-smooth flow fields. *Comput. Vis. Image Underst.*, **63**, 75–104, https://doi.org/10.1006/cviu.1996.0006.

Bluestein, H. B., A. L. Pazmany, J. C. Galloway, and R. E. Mcintosh, 1995: Studies of the substructure of severe convective storms using a mobile 3-mm-wavelength Doppler radar. *Bull. Amer. Meteor. Soc.*, **76**, 2155–2169, https://doi.org/10.1175/1520-0477(1995)076<2155:SOTSOS>2.0.CO;2.

——, M. M. French, I. Popstefanija, R. T. Bluth, and J. B. Knorr, 2010: A mobile, phased-array doppler radar for the study of severe convective storms: The MWR-05XP. *Bull. Amer. Meteor. Soc.*, **91**, 579–600, https://doi.org/10.1175/2009BAMS2914.1.

Brandes, E. A., 1977: Gust front evolution and tornado genesis as viewed by Doppler radar. *J. Appl. Meteor.*, **16**, 333–338, https://doi.org/10.1175/1520-0450(1977)016<0333:GFEATG>2.0.CO;2.

——, 1978: Mesocyclone evolution and tornadogenesis: Some observations. *Mon. Wea. Rev.*, **106**, 995–1011, https://doi.org/10.1175/1520-0493(1978)106<0995:MEATSO>2.0.CO;2.

——, 1984: Vertical vorticity generation and mesocyclone sustenance in tornadic thunderstorms: The observational evidence. *Mon. Wea. Rev.*, **112**, 2253–2269, https://doi.org/10.1175/1520-0493(1984)112<2253:VVGAMS>2.0.CO;2.

Bresky, W. C., J. M. Daniels, A. A. Bailey, and S. T. Wanzong, 2012: New methods toward minimizing the slow speed bias associated with atmospheric motion vectors. *J. Appl. Meteor. Climatol.*, **51**, 2137–2151, https://doi.org/10.1175/JAMC-D-11-0234.1.

Browning, K. A., 1964: Airflow and precipitation trajectories within severe local storms which travel to the right of the winds. *J. Atmos. Sci.*, **21**, 634–639, https://doi.org/10.1175/1520-0469(1964)021<0634:AAPTWS>2.0.CO;2.

——, 1965: Some inferences about the updraft within a severe local storm. *J. Atmos. Sci.*, **22**, 669–677, https://doi.org/10.1175/1520-0469(1965)022<0669:SIATUW>2.0.CO;2.

Brox, T., 2005: From pixels to regions: Partial differential equations in image analysis. Ph.D. thesis, Saarland University, 202 pp.

——, A. Bruhn, N. Papenberg, and J. Weickert, 2004: High accuracy optical flow estimation based on a theory for warping. *Eighth European Conf. on Computer Vision*, Vol. 4, Prague, Czech Republic, ECCV, 25–36.

Brunner, J. C., S. A. Ackerman, A. S. Bachmeier, and R. M. Rabin, 2007: A quantitative analysis of the enhanced-V feature in relation to severe weather. *Wea. Forecasting*, **22**, 853–872, https://doi.org/10.1175/WAF1022.1.

Bryan, G. H., J. C. Wyngaard, and J. M. Fritsch, 2003: Resolution requirements for the simulation of deep moist convection. *Mon. Wea. Rev.*, **131**, 2394–2416, https://doi.org/10.1175/1520-0493(2003)131<2394:RRFTSO>2.0.CO;2.

Bunkers, M. J., B. A. Klimowski, J. W. Zeitler, R. L. Thompson, and M. L. Weisman, 2000: Predicting supercell motion using a new hodograph technique. *Wea. Forecasting*, **15**, 61–79, https://doi.org/10.1175/1520-0434(2000)015<0061:PSMUAN>2.0.CO;2.

Butler, D. J., J. Wulff, G. B. Stanley, and M. J. Black, 2012: A naturalistic open source movie for optical flow evaluation. *12th European Conf. on Computer Vision*, Florence, Itlay, ECCV, 611–625, https://doi.org/10.1007/978-3-642-33783-3_44.

Byers, H. R., and R. R. Braham Jr., 1949: *The Thunderstorm*. U.S. Government Printing Office, 287 pp.

Carr, J. L., D. L. Wu, M. A. Kelly, and J. Gong, 2018: MISR-GOES 3D winds: Implications for future LEO-GEO and LEO-LEO winds. *Remote Sens.*, **10**, 1885, https://doi.org/10.3390/rs10121885.

Dahl, J. M. L., M. D. Parker, and L. J. Wicker, 2012: Uncertainties in trajectory calculations within near-surface mesocyclones of simulated supercells. *Mon. Wea. Rev.*, **140**, 2959–2966, https://doi.org/10.1175/MWR-D-12-00131.1.

Davies-Jones, R. P., R. J. Trapp, and H. B. Bluestein, 2001: Tornadoes and tornadic storm. *Severe Convective Storms*, Meteor. Monogr., No. 28, Amer. Meteor. Soc., 167–221.

Deierling, W., and W. A. Petersen, 2008: Total lightning activity as an indicator of updraft characteristics. *J. Geophys. Res.*, **113**, D16210, https://doi.org/10.1029/2007JD009598.

Fleet, D., and Y. Weiss, 2005: Optical flow estimation. *Handbook of Mathematical Model in Computer Vision*, N. Paragios, Y. Chen, and O. D. Faugeras, Eds., Springer, 237–257, https://doi.org/10.1109/TIP.2009.2032341.

Fortun, D., P. Bouthemy, C. Kervrann, D. Fortun, P. Bouthemy, and C. Kervrann, 2015: Optical flow modeling and computation: A survey. *Comput. Vis. Image Underst.*, **134**, 1–21, https://doi.org/10.1016/j.cviu.2015.02.008.

French, M. M., H. B. Bluestein, I. PopStefanija, C. A. Baldi, and R. T. Bluth, 2014: Mobile, phased-array, Doppler radar observations of tornadoes at X Band. *Mon. Wea. Rev.*, **142**, 1010–1036, https://doi.org/10.1175/MWR-D-13-00101.1.

Fujita, T. T., 1968: Present status of cloud velocity computations from ATS-1 and ATS-3. *Ninth Plenary Meeting on Space Research*, Tokyo, Japan, COSPAR, 557–570.

——, 1982: Principle of stereoscopic height computations and their applications to stratospheric cirrus over severe thunderstorms. *Kisho Shushi. Daishu*, **60**, 355–368.

Geiger, A., P. Lenz, and R. Urtasun, 2012: Are we ready for autonomous driving? The KITTI vision benchmark suite. *2012 IEEE Conf. on Computer Vision and Pattern Recognition*, Providence, RI, IEEE, 3354–3361, https://doi.org/10.1109/CVPR.2012.6248074.

Griffin, S. M., K. M. Bedka, and C. S. Velden, 2016: A method for calculating the height of overshooting convective cloud tops using satellite-based IR imager and *CloudSat* cloud profiling radar observations. *J. Appl. Meteor. Climatol.*, **55**, 479–491, https://doi.org/10.1175/JAMC-D-15-0170.1.

Hasler, A. F., 1981: Stereographic observations from geosynchronous satellites: An important new tool for the atmospheric sciences. *Bull. Amer. Meteor. Soc.*, **62**, 194–212, https://doi.org/10.1175/1520-0477(1981)062<0194:SOFGSA>2.0.CO;2.

——, J. Strong, R. H. Woodward, and H. Pierce, 1991: Automatic analysis of stereoscopic satellite image pairs for Determination of cloud-top height and structure. *J. Appl. Meteor.*, **30**, 257–281, https://doi.org/10.1175/1520-0450(1991)030<0257:AAOSSI>2.0.CO;2.

Heidinger, A. K., 2013: Algorithm theoretical basis document: ABI cloud height. NOAA/NESDIS, 79 pp., https://www.star.nesdis.noaa.gov/goesr/docs/ATBD/Cloud_Height.pdf.

Helmus, J. J., and S. M. Collis, 2016: The Python ARM Radar Toolkit (Py-ART), a library for working with weather radar data in the Python programming language. *J. Open Res. Software*, **4**, e25, https://doi.org/10.5334/jors.119.

Homeyer, C. R., J. D. McAuliffe, and K. M. Bedka, 2017: On the development of above-anvil cirrus plumes in extratropical convection. *J. Atmos. Sci.*, **74**, 1617–1633, https://doi.org/10.1175/JAS-D-16-0269.1.

Horn, B. K. P., and B. G. Schunck, 1981: Determining optical flow. *Artif. Intell.*, **17**, 185–203, https://doi.org/10.1016/0004-3702(81)90024-2.

Klemp, J. B., 1987: The dynamics of severe thunderstorms. *Annu. Rev. Fluid Mech.*, **19**, 369–402, https://doi.org/10.1146/annurev.fl.19.010187.002101.

——, R. B. Wilhelmson, and P. S. Ray, 1981: Observed and numerically simulated structure of a mature supercell thunderstorm. *J. Atmos. Sci.*, **38**, 1558–1580, https://doi.org/10.1175/1520-0469(1981)038<1558:OANSSO>2.0.CO;2.

Kumjian, M. R., and A. V. Ryzhkov, 2008: Polarimetric signatures in supercell thunderstorms. *J. Appl. Meteor. Climatol.*, **47**, 1940–1961, https://doi.org/10.1175/2007JAMC1874.1.

Lemon, L. R., and C. A. Doswell, 1979: Severe thunderstorm evolution and mesocyclone structure as related to tornadogenesis. *Mon. Wea. Rev.*, **107**, 1184–1197, https://doi.org/10.1175/1520-0493(1979)107<1184:STEAMS>2.0.CO;2.

Mansell, E. R., C. L. Ziegler, and E. C. Bruning, 2010: Simulated electrification of a small thunderstorm with two-moment bulk microphysics. *J. Atmos. Sci.*, **67**, 171–194, https://doi.org/10.1175/2009JAS2965.1.

Markowski, P. M., 2002: Hook echoes and rear-flank downdrafts: A review. *Mon. Wea. Rev.*, **130**, 852–876, https://doi.org/10.1175/1520-0493(2002)130<0852:HEARFD>2.0.CO;2.

Marwitz, J. D., 1972: The structure and motion of severe hailstorms. Part I: Supercell storms. *J. Appl. Meteor.*, **11**, 166–179, https://doi.org/10.1175/1520-0450(1972)011<0166:TSAMOS>2.0.CO;2.

Mashiko, W., H. Niino, and T. Kato, 2009: Numerical simulation of tornadogenesis in an outer-rainband minisupercell of Typhoon Shanshan on 17 September 2006. *Mon. Wea. Rev.*, **137**, 4238–4260, https://doi.org/10.1175/2009MWR2959.1.

McCann, D. W., 1983: The enhanced-V: A satellite observable severe storm signature. *Mon. Wea. Rev.*, **111**, 887–894, https://doi.org/10.1175/1520-0493(1983)111<0887:TEVASO>2.0.CO;2.

Mecikalski, J. R., T. N. Sandmæl, E. Murillo, C. R. Homeyer, K. M. Bedka, J. M. Apke, and C. P. Jewett, 2021: A random-forest model to assess predictor importance and nowcast severe storms using high-resolution radar-GOES satellite-lightning observations. *Mon. Wea. Rev.*, **149**, 1725–1746, https://doi.org/10.1175/MWRD-19-0274.1.

NCEI, 2021: NOAA National Centers for Environmental Information archived information request system. Accessed 1 March 2021, https://www.ncei.noaa.gov/.

Nieman, S. J., W. P. Menzel, C. M. Hayden, D. Gray, S. T. Wanzong, C. S. Velden, and J. Daniels, 1997: Fully automatic cloud drift winds in NESDIS operations. *Bull. Amer. Meteor. Soc.*, **78**, 1121–1133, https://doi.org/10.1175/1520-0477(1997)078<1121:FACDWI>2.0.CO;2.

Oye, R., C. Mueller, and S. Smith, 1995: Software for radar translation, visualization, editing, and interpolation. Preprints, *27th Conf. on Radar Meteorology*, Vail, CO, Amer. Meteor. Soc., 359–361.

Rotunno, R., and J. B. Klemp, 1982: The influence of the shear-induced pressure gradient on thunderstorm motion. *Mon. Wea. Rev.*, **110**, 136–151, https://doi.org/10.1175/1520-0493(1982)110<0136:TIOTSI>2.0.CO;2.

——, and ——, 1985: On the rotation and propagation of simulated supercell thunderstorms. *J. Atmos. Sci.*, **42**, 271–292, https://doi.org/10.1175/1520-0469(1985)042<0271:OTRAPO>2.0.CO;2.

Sandmæl, T. N., C. R. Homeyer, K. M. Bedka, J. M. Apke, J. R. Mecikalski, and K. Khlopenkov, 2019: Evaluating the ability of remote sensing observations to identify significantly severe and potentially tornadic storms. *J. Appl. Meteor. Climatol.*, **58**, 2569–2590, https://doi.org/10.1175/JAMC-D-18-0241.1.

Schenkman, A. D., M. Xue, and M. Hu, 2014: Tornadogenesis in a high-resolution simulation of the 8 May 2003 Oklahoma City

supercell. *J. Atmos. Sci.*, **71**, 130–154, https://doi.org/10.1175/JAS-D-13-073.1.

Schmit, T. J., P. Griffith, M. M. Gunshor, J. M. Daniels, S. J. Goodman, and W. J. Lebair, 2017: A closer look at the ABI on the GOES-R series. *Bull. Amer. Meteor. Soc.*, **98**, 681–698, https://doi.org/10.1175/BAMS-D-15-00230.1.

Schultz, C. J., W. A. Petersen, and L. D. Carey, 2009: Preliminary development and evaluation of lightning jump algorithms for the real-time detection of severe weather. *J. Appl. Meteor. Climatol.*, **48**, 2543–2563, https://doi.org/10.1175/2009JAMC2237.1.

——, W. Petersen, and L. D. Carey, 2011: Lightning and severe weather: A comparison between total and cloud-to-ground lightning trends. *Wea. Forecasting*, **26**, 744–755, https://doi.org/10.1175/WAF-D-10-05026.1.

——, L. D. Carey, E. V. Schultz, and R. J. Blakeslee, 2015: Insight into the kinematic and microphysical processes that control lightning jumps. *Wea. Forecasting*, **11**, 1591–1621, https://doi.org/10.1175/WAF-D-14-00147.1.

Shi, J., and Tomasi, 1994: Good features to track. *Proc. IEEE Conf. on Computer Vision and Pattern Recognition*, Seattle, WA, IEEE, 593–600, https://doi.org/10.1109/CVPR.1994.323794.

Skamarock, W. C., and Coauthors, 2008: A description of the Advanced Research WRF version 3. NCAR Tech. Note NCAR/TN-475+STR, 113 pp., https://doi.org/10.5065/D68S4MVH.

Smagorinsky, J., 1963: General circulation experiments with the primitive equations. *Mon. Wea. Rev.*, **91**, 99–164, https://doi.org/10.1175/1520-0493(1963)091<0099:GCEWTP>2.3.CO;2.

Smolarkiewicz, P., and R. Rotunno, 1989: Low Froude number flow past three-dimensional obstacles. Part I: Baroclinically generated lee vortices. *J. Atmos. Sci.*, **46**, 1154–1164, https://doi.org/10.1175/1520-0469(1989)046<1154:LFNFPT>2.0.CO;2.

Stough, S. M., L. D. Carey, C. J. Schultz, and P. M. Bitzer, 2017: Investigating the relationship between lightning and mesocyclonic rotation in supercell thunderstorms. *Wea. Forecasting*, **32**, 2237–2259, https://doi.org/10.1175/WAF-D-17-0025.1.

Sun, D., S. Roth, and M. J. Black, 2014: A quantitative analysis of current practices in optical flow estimation and the principles behind them. *Int. J. Comput. Vis.*, **106**, 115–137, https://doi.org/10.1007/s11263-013-0644-x.

Sundaram, N., T. Brox, and K. Keutzer, 2010: Dense point trajectories by GPU-accelerated large displacement optical flow. *11th European Conf. on Computer Vision*, Heraklion, Greece, ECCV, 438–451, https://doi.org/10.1007/978-3-642-15549-9_32.

Wang, P. K., 2003: Moisture plumes above thunderstorm anvils and their contributions to cross-tropopause transport of water vapor in midlatitudes. *J. Geophys. Res.*, **108**, 4194, https://doi.org/10.1029/2002JD002581.

——, 2004: A cloud model interpretation of jumping cirrus above storm top. *Geophys. Res. Lett.*, **31**, L18106, https://doi.org/10.1029/2004GL020787.

——, 2007: The thermodynamic structure atop a penetrating convective thunderstorm. *Atmos. Res.*, **83**, 254–262, https://doi.org/10.1016/j.atmosres.2005.08.010.

——, K. Cheng, M. Setvak, and C. Wang, 2016: The origin of the gullwing-shaped cirrus above an Argentinian thunderstorm as seen in CALIPSO images. *J. Geophys. Res. Atmos.*, **121**, 3729–3738, https://doi.org/10.1002/2015JD024111.

Weisman, M. L., and J. B. Klemp, 1982: The dependence of numerically simulated convective storms on vertical wind shear and buoyancy. *Mon. Wea. Rev.*, **110**, 504–520, https://doi.org/10.1175/1520-0493(1982)110<0504:TDONSC>2.0.CO;2.

——, and ——, 1984: The structure and classification of numerically simulated convective storms in directionally varying wind shears. *Mon. Wea. Rev.*, **112**, 2479–2498, https://doi.org/10.1175/1520-0493(1984)112<2479:TSACON>2.0.CO;2.

Wicker, L. J., and R. B. Wilhelmson, 1995: Simulation and analysis of tornado development and decay within a three-dimensional supercell thunderstorm. *J. Atmos. Sci.*, **52**, 2675–2703, https://doi.org/10.1175/1520-0469(1995)052<2675:SAAOTD>2.0.CO;2.

Williams, E., and Coauthors, 1999: The behavior of total lightning activity in severe Florida thunderstorms. *Atmos. Res.*, **51**, 245–265, https://doi.org/10.1016/S0169-8095(99)00011-3.

Wurman, J., J. Straka, E. Rasmussen, M. Randall, and A. Zahrai, 1997: Design and deployment of a portable, pencil-beam, pulsed, 3-cm Doppler radar. *J. Atmos. Oceanic Technol.*, **14**, 1502–1512, https://doi.org/10.1175/1520-0426(1997)014<1502:DADOAP>2.0.CO;2.

Wylie, D. P., D. Santek, and D. O. Starr, 1998: Cloud-top heights from *GOES-8* and *GOES-9* stereoscopic imagery. *J. Appl. Meteor.*, **37**, 405–413, https://doi.org/10.1175/1520-0450(1998)037<0405:CTHFGA>2.0.CO;2.